NTNU
Norwegian University of
Science and Technology

Implementation and Assessment of Supersonic Shear Imaging Techniques

Benjamin Strandli Fermann

Master of Science in Electronics
Submission date: June 2017
Supervisor: Ilangko Balasingham, IES
Co-supervisor: Lasse Løvstakken, ISB, NTNU

Norwegian University of Science and Technology
Department of Electronic Systems

Implementation and Assessment of Supersonic Shear Imaging Techniques

Benjamin Strandli Fermann

June 2017

MASTER THESIS
Department of Electronic Systems
Norwegian University of Science and Technology

Supervisor: Lasse Løvstakken

Preface

This report is the Master's thesis for my degree in Electronics at the Department of Electronic Systems (IES), at the Norwegian University of Science and Technology (NTNU). This master project has been done at the Department of Circulation and Medical Imaging (ISB). The work was done during the spring semester of 2017, and was supervised by Lasse Løvstakken.

Acknowledgment

I would like to thank my supervisor Lasse Løvstakken for all the help and involvement throughout the year. And Alfonso Rodriguez-Molares for his enthusiastic assistance with any and all practical matters. I would also like to thank Sebastien Salles for sharing his code and constructive discussions on the algorithms.

Trondheim, 2017-06-20

Benjamin Strandli Fermann

Sammendrag

Skjærbølge-elastografi er en ultralydsteknikk som kan måle elastisiteten til vev kvantitativt. Teknikken gir verdifull diagnostisk informasjon som kommer i tillegg til konvensjonelle ultralydsteknikker. Skjærbølge-elastografi har vist seg å kunne gi bedre resultater ved identifisering og klassifisering av flere sykdommer som bryst- og prostatakreft. Vevselastisitet er også en verdifull diagnostisk egenskap for sykdommer som ikke har synlige strukturelle anomalier, som for eksempel fibrose. Dett prosjektet hadde som mål å implementere det ypperste innen supersonisk skjæravbildning på en ultralydmaskin for utvikling av Verasonics, og å vurdere resultatene av elastisitetsestimering av ulike vevsetterliknende fantomer. Et oppsett ble utviklet med en lineær ultralydsprobe som eksiterte skjærbølger i vev gjennom akustisk strålingskraft, bølgeforplantningen ble avbildet med plane bølger gjennom ultrakjapp ultralyd, og vevselastisiteten ble estimert som en funksjon av skjærbølgehastigheten. Noen ulike tilnærminger til hastighetsestimering ble implementert og diskutert, en algoritme basert på detektering av linjer ble funnet å være rask, men hadde dårlig oppløsning. En annen metode brukte krysskorrelering for å estimere forplantningen og ga bedre resultater, men var brukte lenger tid. Uavhengig av hvilken metode som ble brukt så viser det seg at det er viktig med et bevisst valg av estimeringsparametre for å få nøyaktige resultater med god kjøretid. Implementasjonen var i stand til å oppdage en myk vevslomme i et heterogent fantom, til tross for ujevnheter i det omkringliggende vevet. Elastiske cyster ble også oppdaget i et flerbruksfantom, med langt bedre kontrast enn tilsvarende B-modus avbildning. Til slutt ble et oppsett med to ultralydsprober implementert, der en brukes til å generere skjærbølger, mens den andre brukes til avbildning.

Abstract

Shear Wave Elastography (SWE) is an ultrasound modality which can measure tissue elasticity quantitatively. It provides valuable diagnostic information in addition to conventional ultrasound modalities. SWE has been shown to provide improved performance for detection and classification of several diseases, such as breast and prostate cancer. Tissue elasticity is also a valuable diagnostic property for diffuse diseases that don't have any visible structural anomalies, such as fibrosis. This project aimed to implement state-of-the-art in Supersonic Shear Imaging (SSI) on a Verasonics ultrasound research system, and to assess the performance of the elasticity estimation on various tissue-mimicking phantoms. A setup was developed with a linear array transducer to excite shear waves in tissue using acoustic radiation force, the propagation of the waves were imaged using plane wave ultrafast ultrasound and the tissue elasticity was estimated as a function of the shear wave velocity. A few different approaches to the velocity estimation were implemented and discussed, an algorithm based on line detection was found to be fast, but with poor resolution. While a method using cross-correlations to estimate propagation provided better velocity maps, but was considerably slower. With either approach it is found that careful choice of estimation parameters is necessary to provide good performance in terms of accuracy and efficiency. The implementation was able detect a soft cyst in a heterogeneous phantom despite irregularities in the surrounding medium. Elastic cysts were also detected in a multi-purpose phantom, with far better contrast than the B-mode equivalent. Finally, a setup using two ultrasound transducers was implemented, using one transducer to generate shear waves and the other for imaging.

Abbreviations and frequently used symbols

Abbreviations

ARF Acoustic Radiation Force

ARFI Acoustic Radiation Force Impulse

CT Computed Tomography

FPS Frames Per Second

IES Department of Electronic Systems (Institutt for elektroniske systemer)

ISB Department of Circulation and Medical Imaging (Institutt for sirkulasjon og bildediagnostikk)

LoG Laplacian of Gaussian

MI Mechanical Index

MRI Magnetic Resonance Imaging

NTNU Norwegian University of Science and Technology (Norges teknisk-naturvitenskapelige universitet)

PRF Pulse Repetition Frequency

PVA Polyvinyl alcohol

ROI Region of Interest

SNR Signal-to-Noise Ratio

SSI Supersonic Shear Imaging

SWE Shear Wave Elastography

TDI Tissue Doppler Imaging

TI Thermal Index

US Ultrasound

Frequently used symbols

c	Speed of sound in tissue [m/s]
λ	Wavelength [m]
Z	Acoustic impedance [Pa·s/m^3]
Γ	Reflection coefficient
c_t	Shear wave velocity [m/s]
ρ	Mass density [kg/m^3]
μ	Shear modulus [Pa]
E	Young's modulus [Pa]
ν	Poisson's ratio
σ	Standard deviation
$r_{xy}(\tau)$	Cross-correlation function
τ	Time delay in pixels, used in cross-correlation function

Contents

Chapter 1

Introduction

This chapter introduces the technical problem at hand along with a medical motivation. The goals of the project are presented and a brief overview of the techniques and history of the ultrasound field is given.

1.1 Problem Statement

Tissue stiffness can be used as an indicator for the presence and classification of cancer tumors and diffuse diseases like liver fibrosis. Shear Wave Elastography (SWE) methods use ultrasound techniques to image this tissue stiffness, and provides valuable diagnostic information in addition to conventional ultrasound. Ultrasound is a cheap, portable and non-intrusive diagnostic imaging modality, which makes SWE techniques very desirable as a diagnostic tool.

This project aims to assess the capabilities of Supersonic Shear Imaging (SSI) through comparison of different sequences in both homogeneous and heterogeneous mediums. Different post-processing methods will be presented and used to estimate the shear wave velocity, which is an excellent estimator for tissue stiffness. Additionally this project will demonstrate the feasibility of an SSI method using two US probes for imaging.

1.2 Objectives

The main objectives of this project are:

- Implement SSI on a Verasonics ultrasound research system and assess its performance on various phantoms.
- Implement a robust and efficient shear wave velocity estimation algorithm.

- Assess the feasibility of dual transducer setups for SWE methods

1.3 Limitations

This project is limited to *in vitro* tests on tissue-mimicking phantoms. A brief assessment of the thermal output during operation is presented, but the methods will not be used *in vivo*. In general, clinical safety is outside the scope of this project and will need to be thoroughly assessed before the *in vivo* performance can be assessed.

1.4 Ultrasound

Just like regular sound, ultrasound is acoustic pressure waves, but at a higher frequency. The use of sound waves for echo-localization has existed in nature for a long time (e.g. bats), as a technology it was first used in what would evolve to be known as SONAR systems (SOund Navigation And Ranging). This development started in 1912 and the research was in large parts driven by a desire to locate submarines and icebergs underwater [2]. In 1942, Karl Dussik [3] first used ultrasound to image tissue. He used a setup similar to x-rays, where he transmitted ultrasound through a head with the receiver on the other side. By the end of the 40s, researchers had instead begun using the reflected ultrasound. The 50s saw the development of the first B-mode scanner, and blood flow estimates through continuous wave Doppler techniques. By the early 60s, most of the fundamental concepts in diagnostic ultrasound had been demonstrated [4]. While some of the most basic US techniques can be performed with analog equipment, all modern US techniques rely heavily on digital signal processing. As a result, the development of ultrasound techniques and equipment is closely related to the developments in electronics hardware. Pulsed wave Doppler and color flow imaging are two examples of US modalities developed in the 80s that were only made possible by hardware developments. Today, the miniaturization of electronics and developments in computational performance has made US one of the most affordable and portable imaging technologies.

Other diagnostic imaging modalities used today include Computed Tomography (CT), Magnetic Resonance Imaging (MRI) and plain radiography (x-rays) as the most common modalities. Unlike US, plain radiography is not capable of distinguishing soft tissue, but can detect bones and air. As a result, there is not much overlap between the use cases of US and plain radiography. Ultrasound is also a safer option than both plain radiography and CT, as they both use ionizing radiation which can be harmful. CT scans the body at different angles in order to provide a three-dimensional image of the body, usually represented as a series of 2D images. This volumetric resolution offers more information about soft tissue than just plain radiography. CT is also considerably more expensive than US, image acquistion is time consuming and requires the patient to lay still during the acquisition. MRI does not subject the patient to any harmful radiation, and offers excellent soft tissue imaging. However, MRI equipment is very expensive and because of the strong magnetic field, the entire room needs to be built with MRI in mind. The low cost, high portability, ease of use provided by the real-time capabilities, and the ability to image movement of organs, all contribute to making US the second most common imaging modality, after x-rays. [5], [6]

1.5 Ultrasound elastography

Manual palpation with fingers has been used as a diagnostic tool for identifying shallow cancer tumors for centuries[7]. The stiffness experienced through palpation is the same property that elastography aims to visualize, sonoelastography, or ultrasound elastography uses ultrasound to perform the imaging. The ability to perform "remote palpation" is valuable because it provides additional information to conventional ultrasound, and is also intuitive because of the direct relation to the experience from manual palpation. Compared to conventional ultrasound, sonoelastography provides better contrast in cases where the difference in elasticity is great, but not the acoustic impedance. An example is prostate cancer where elastography has been shown to improve detection over regular US [8], [9]. Quantitative elasticity estimates are particularly valuable in diagnosis of diffuse diseases like liver fibrosis, where the disease is not localized in a way where it can be compared to the surrounding tissue [10]. It has also been used to improve the accuracy when differentiating between malignant and benign breast masses [11]–[13].

Initial assessments of the elastic properties of tissue were made in 1951 by Hans Oestreicher [14] who identified relations between transversal waves and the shear elasticity of a viscoelastic medium. Ultrasound imaging of these elastic properties were presented in 1987 by Robert M. Lerner [15] as *vibration amplitude sonoelastography.* The method was based on exciting low-frequency vibrations externally into tissue, regions with different stiffness would cause a different frequency response which could be detected through Doppler methods. A similar method called *vibration phase gradient sonoelastography* [16] also mapped the phase of the vibrations, making it possible to derive the wave propagation velocity which are closely related to the elastic properties. Yet another method, *radiation force vibration acoustography* is based on measuring the displacement of tissue caused by an ultrasound beam. The absorption of the ultrasound will vary with tissue properties and will cause a radiation force which will lead to deformation of tissue. The amplitude and relaxation time of this tissue displacement can then be used as estimators for the elastic properties [17], [18].

Shear wave elastography (SWE) as it was presented by Sarvazyan in 1998 [19] differed from the previous methods by using shorter, focused impulses, rather than continuous vibrations, to cause displacement and shear waves in tissue. This gave the ability to excite shear waves at an arbitrary point in tissue, which also provides good localized estimates. Three estimators were suggested for estimations of the elasticity: the maximum axial displacement at the focal point, the time until maximum axial displacement, and the velocity of the generated shear wave. Using the shear wave velocity as an estimator has the benefit that estimations can be made over an area beyond the focal point, and it is a quantitative estimator. Methods using the propagation of these shear waves are also known as *transient elastography* techniques. It was also suggested that excitation and imaging could be done with the same US probe, without the need for an external vibrator. This single probe setup was implemented by Nightingale in 2001 [1]. Using an US probe to generate long, high energy pulses capable of exciting tissue, known as *acoustic radiation force impulse* (ARFI), was also used in a new method called superonic shear imaging (SSI). SSI relies on the low velocities of shear waves to focus several ARFI pulses along a line in quick succession and achieve a virtual shear wave source moving at "supersonic" speeds, relative to the shear wave velocities. The series of pushes must be placed with distances between each focal point large enough that the virtual source moves faster than the shear waves, this generates a "mach-cone", a quasi-plane wavefront caused by the constructive interference of the individual ARFI pushes. The benefit of SSI is that it can cover a larger area in just one sequence, while also providing quantitative estimates[20].

1.6 Structure of the Report

Chapter 2 will discuss the technical background for the project and describe the physical and mathematical principles used. Chapter 3 presents the methodology for the measurements, post-processing and the production of the ultrasound phantom. Chapter 4 contains the results, which will be discussed in Chapter. Finally, Chapter 6 will summarize the work in a conclusion.

Chapter 2

Theory

This chapter presents the technical background for the ultrasound and post-processing techniques used in this project.

2.1 General ultrasound

Ultrasound (US) refers to acoustic waves at frequencies beyond human hearing, typically in the range of 1-10 MHz for medical imaging applications. These waves have longitudinal propagation, which means the direction of vibration (of individual particles) is the same as the direction of propagation, as shown in Figure 2.1a. In tissue these waves propagate at a mostly constant velocity of ~1540 m/s, and are reflected whenever there is a change in the acoustical impedance of the tissue. The acoustic impedance, Z, is an intrinsic property of the tissue and is directly related to other properties such as mass density, ρ, and speed of sound, c as shown in (2.1). Speed of sound can in turn be expressed as a function of mass density and volume compressibility, κ.

$$Z = \rho c = \sqrt{\frac{\rho}{\kappa}} \tag{2.1}$$

The relative amplitude of the reflected signal increases with the difference in acoustic impedance and is described by the reflection coefficient, Γ. For an acoustical wave propagating from a medium with acoustic impedance Z_1 to Z_2, the reflection coefficient is given by:

$$\Gamma = \frac{Z_2 - Z_1}{Z_2 + Z_1} \tag{2.2}$$

This reflection coefficient shows that it's possible to transmit ultrasound signals into tissue, record the signals reflected back in the tissue, and use this to obtain information about the acoustic properties of the tissue. The corresponding depth of a received reflected signal is proportional to the time delay of the signal, under the assumption that speed of sound is relatively constant. This depth, d, is given by the relation in (2.3) where c is speed of sound, and t is the time delay between the transmitted and received signal.

$$d = \frac{ct}{2} \tag{2.3}$$

The pulse repetition frequency (PRF), is limited by the time spent per pulse, which we can see from the relation (2.3) is given by the maximum imaging depth as shown in equation (2.4).

$$PRF = \frac{c}{2d_{max}} \tag{2.4}$$

Diagnostic ultrasound typically uses an array of transducer elements made with a piezoelectric material. The piezoelectric effect means that applying voltage to the material will induce mechanical stress, and inversely, mechanical stress will induce electrical voltage. This allows each transducer element to both transmit and receive acoustic pressure waves. In colloquial terms they behave as both loudspeakers and microphones. By using arrays of individual elements it's possible to achieve spatial focus of both the transmitted and received acoustic waves by applying small time delays corresponding to the element position.

2.2 Shear Wave Elastography (SWE)

The elastic properties of tissues provide valuable diagnostic information, but conventional US modalities lack the ability to extract this information. Elastography techniques aim to image this elasticity, to provide additional information about tissue properties. Most elastography techniques aim to provide a quantitative measure of the Young's modulus, which corresponds to the stiffness experienced through palpation. SWE methods typically involve excitation and tracking of shear waves, in order to use the velocity of the shear waves as an estimator for Young's modulus, which is the primary elasticity property of interest.

Unlike the longitudinal acoustic waves generated by the US transducers, shear waves are transversal waves propagating in directions perpendicular to the particle vibration as shown in Figure 2.1b. These shear waves propagate at a velocity far below the speed of sound in soft tissue, velocities are in the range of 0.5-50 m/s [19]. Equations (2.5) and (2.6) show the relations between shear wave velocity c_t, and Young's modulus E [21].

$$c_t = \sqrt{\frac{\mu}{\rho}} \tag{2.5}$$

$$\begin{aligned} E &= 2\mu(1+\nu) \\ &= 2\rho c_t^2(1+\nu) \\ &\approx 3\rho c_t^2 \end{aligned} \tag{2.6}$$

μ is the shear modulus, and ρ is the mass density. Additionally, because biological tissue is nearly incompressible, the Poisson's ratio, ν, approaches 0.5 [22].

(a) Longitudinal waves (compression waves)

(b) Transversal waves

Figure 2.1: Shear waves are transversal waves where the particle displacement is perpendicular to the direction of propagation.

2.2.1 Acoustic Radiation Force Impulsion (ARFI)

ARFI is the fundamental technique in most SWE methods, it involves transmitting a strong ultrasound pulse in order to exert radiation force and induce shear waves in tissue. The acoustic radiation force (ARF) pulses need to be focused to get sufficiently high pressure to exert radiation force, this also allows us to get localized estimates. For a dissipative medium like soft tissue, the radiation force F, is given by:

$$F = \frac{2\alpha I}{c} \tag{2.7}$$

$$I = \frac{\frac{1}{T}\int_0^T p^2 \,\mathrm{d}t}{2\rho c} \tag{2.8}$$

where α is the attenuation coefficient, and I is the local, temporal average intensity of the ultrasound beam. The intensity will have its maximum around the focal point, and is proportional to the square of the pressure field as shown in equation (2.8) [23], where p is the pressure field. In addition to these linear effects, the high pressure in the focal region will generate more high frequency harmonics leading to additional nonlinear absorption [19]. These high energy requirements means that ARF pulses are generated using high voltage and relatively long pulse lengths, 100 µs would be a typical value, but it can vary significantly with application (i.e. 25-800 µs [20], [23]–[26]). Unsurprisingly, the tissue displacement caused by the ARF pulse will be largest in the focal point. Sarvazyan presents the relation between the rise time until maximum displacement t_{max}, and the shear modulus μ as:

$$\mu = \rho\left(\frac{aD}{t_{max}}\right) \tag{2.9}$$

where D is a diffraction parameter, and a is a parameter related to the width of the Gaussian profile of the ultrasound beam in axial direction [19]. In practice, it may be difficult to get quantitative estimates this way because a perfectly Gaussian beam profile might not be a reasonable assumption. The elasticity estimate will also be limited to the focal point. Instead, the excited shear waves can be tracked, and elasticity can be estimated in the region the wave passes through based on its velocity. In order to achieve this it's necessary to use ultrafast ultrasound techniques capable of sampling the phase changes of the shear waves. Conventional US imaging transmits several focused beams in order to get localized information and combines them to one image, which means that the frame rate is limited by the number of pulses per frame. Shear wave frequencies are typically between 500 Hz and 1000 Hz, and the sampling rate needs to be twice that to satisfy the Nyquist limit, this is beyond the capabilities of regular US [27]. Utrafast US on the other hand, transmits unfocused beams and beamforms the received signal to create a complete image. The lack of transmit focus does reduce SNR, but it also means the frame rate is now only limited by the PRF. It's also possible to improve the image quality of ultrafast US by steering the plane pulses in different directions and use compounding of multiple frames to improve image quality. Best compounding performance is achieved when the frames are compounded coherently, based on the pressure field rather than the intensity image [28].

2.2.2 Supersonic Shear Imaging (SSI)

Supersonic Shear Imaging (SSI) is an extension of the SWE method, using ARF pulses to generate shear waves, and ultrafast ultrasound to track them [20]. Instead of simply transmitting one ARF pulse at a time, SSI transmits multiple ARF pulses in quick succession, with slightly different focal points. By focusing in a line along the axial direction, the generated shear waves cover a larger area, making it possible to estimate shear wave velocity in a large area in just one sequence. The individual ARF pulses will generate shear waves that interfer constructively with each other, this is possible because the shear wave velocity is much lower than the speed of sound. If the distance and time intervals between two subsequent ARF pulses correspond to a velocity greater than the shear wave velocity, the interference pattern will create a plane wavefront. Moving the focal point of ARF pulses, is in this case a matter of moving a virtual shear wave source, and a source moving at supersonic speeds will create a Mach-cone. Because the source is moving faster than the shear waves, it is considered to be supersonic and will generate a Mach-cone with a plane, or semi-plane wavefront. The wavefront will have an angle relative to the beam axis given by (2.10) [29]:

$$sin(\theta) = \frac{c_t}{v_{src}} = \frac{1}{M} \tag{2.10}$$

Where θ is the angle of the wavefront, v_{src} is the velocity of the shear wave source (given by the focal points), and M is the Mach number which gives the ratio of source velocity to speed of sound (or speed of shear waves in this case). The velocity of the source is given by the distance between subsequent pushes Δz_{src}, and the PRF PRF_{ARFI} as shown in equation (2.11). The relation between the push intervals and the resulting angle of the wavefront is then given by equation (2.12).

$$v_{src} = \Delta z_{src} PRF_{ARFI} \tag{2.11}$$

$$\Delta z_{src} = \frac{c_t}{PRF_{\text{ARFI}} \sin\theta} = \frac{c_t M}{PRF_{\text{ARFI}}} \tag{2.12}$$

2.3 Post-processing

SWE relies on identifying transversal shear waves and estimating their velocity. This is a complex task which makes it a challenge to produce accurate estimations with efficient methods. There are many different aspects and approaches to this problem, some of which will be presented here. The post-processing methods are described in reasonable detail to illustrate the purpose, even though the core concepts may be implemented in many different variations.

2.3.1 Imaging sequence

With conventional ultrasound methods, each frame is constructed as a combination of multiple acquisition lines. The transmitted ultrasound is beamformed along a line, by adding time delays to the individual transducer elements corresponding to the distance to the focal point as given by equation (2.3). The beamforming limits the influence of tissue outside the relevant region on the received signal, which is again beamformed in the same manner. A series of line acquisitions are then combined to form one frame, this limits the frame rate based on the PRF given by equation (2.4), but also the number of acquisitions used per frame.

When tracking the propagtion of shear waves using SWE, the frame rate needs to be high enough to satisfy the Nyquist limit of the shear wave frequencies. Considering that typical shear wave frequencies are in the range of 500 Hz to 2000 Hz, the corresponding frame rates would need to be at least 1000 Hz to 4000 Hz [27]. This is not possible to achieve with any significant amount of line acquisitions. Instead unfocused, plane waves are transmitted to insonify the entire region in one pulse. This method is called ultrafast ultrasound and is capable of a frame rate equal to the PRF, although the plane waves mean that the ultrasound energy at each point is lower than it would be for focused transmission. Additionally, it's more computationally demanding than conventional US considering an entire frame is reconstructed through beamforming for each acquisition, rather than just a line.

A common method to improve the imaging quality of plane wave US is to use angle compounding. By steering the plane waves in different directions using time delays, it's possible to add the signals from multiple acquisitions with different insonifications to improve image quality. "Incoherent" compounding uses addition of the intensity images from each acquisition to reduce speckle noise and other artifacts. "Coherent" compounding uses the pressure field rather than the intensity, and has been shown to be capable of improving the shear wave velocity estimates [30]. It also improves B-mode image quality and achieves the same quality as conventional methods, but with 10 times fewer insonifications [28]. "Moving" compounding is used to keep the high frame rate even though each frame is combined from several, this means that if each compounded frame is based on N acquisitions, each acquisition is also used in N compounded frames.

2.3.2 Tissue Doppler Imaging

A mechanical shear wave induced in tissue is a transversal wave, which means that the displacement of the tissue is perpendicular to the direction of propagation. For shear waves induced with ARFI with a single transducer, this tissue displacement is in the axial direction. Because of the slow propagation velocities of shear waves, we can use Doppler techniques to measure the tissue displacement.

A Doppler shift occurs whenever a transmitter or receiver is in motion. If the signal source is moving towards the receiver, this will cause a positive frequency shift given by the equation:

$$f_d = f_0 + \Delta f = f_0(1 + \frac{v}{c}) \tag{2.13}$$

Where f_d is the perceived frequency at the receiver, f_0 is the transmitted frequency, Δf is the Doppler shift, c is the speed of sound in the medium, and v is the velocity of the transmitter towards the receiver. Considering the two-way Doppler shift for a scatterer, acting as both a receiver and transmitter, we get the following relation for positive velocity towards the transducer:

$$f_d = f_0 \frac{c + v}{c - v} \approx f_0 + 2\Delta f \tag{2.14}$$

The approximation is reasonable assuming that $v \ll c$. The signal received from a moving scatterer can also be seen as a phase-shifted signal, for practical implementations, we instead use this phase shift to measure velocity. This phase-shift can be found through auto-correlation [31], [32]:

$$R_1 = \sum_{k=1}^{N} z_k \cdot z_{k+1}^* \tag{2.15}$$

$$\Delta f = \frac{\angle R_1 PRF}{2\pi} \tag{2.16}$$

$$v_{tissue} = \frac{\angle R_1 PRF c}{4\pi f_0} \tag{2.17}$$

Equation (2.15) gives R_1 as auto-correlation with a lag of 1, computed by summation of the complex conjugate multiplication of consecutive frames. The angle of this complex value represents the phase-shift between individual frames and can be used to find the Doppler-shifted frequency (2.16), where PRF is the pulse repetition frequency of the imaging sequences. Using the relation in (2.14) and assuming that the tissue velocity is much smaller than the speed of sound, $v_{tissue} \ll c$, and that the velocity is in the axial direction, we find the tissue velocity given by equation (2.17). This velocity is proportional to the amplitude of the shear waves and is useful to detect the wavefront.

2.3.3 Line detection

One method of estimating shear wave velocity is to consider the TDI velocity map in lateral-time direction (x-t plane) at each depth and use a line detection algorithm to identify the shear waves. The corresponding velocity can be found as a function of the slope of the line. The line is first found using edge detection techniques. Edge detection typically involves convolving the image with a filter designed to emphasize the edge features in some way. There are many filters designed for this purpose, with different pros and cons depending on the nature of the data and performance requirements [33]. The Laplacian of Gaussian (LoG) filter is an edge detection filter, and by applying the LoG filter to the TDI map, the edges will be detected and represented as zero-crossings in the resulting image.

A gaussian filter is useful to mask noise, and the variance of the filter can be chosen to correspond well with the width of the edges. This is a very useful property as the shear waves can be quite wide. If we assume that an edge is a location with a very abrupt change, it follows that this would correspond to a zero-crossing in the spatial double derivative. In order to get a two-dimensional double derivative, we can use the Laplacian to create a LoG-filter as defined in (2.18)[34].

$$\nabla^2 G(r) = -\frac{1}{\pi\sigma^4}\left[1 - \frac{r^2}{2\sigma^2}\right] e^{-\frac{r^2}{2\sigma^2}} \tag{2.18}$$

∇ is the Laplacian operator, G is the Gaussian function, r is the radius in polar coordinates and σ is the standard deviation of the Gaussian function. The LoG filter has the advantage that the Laplacian can be applied directly to the Gaussian filter, which provides good computational performance [33]. However the edge detection could potentially be improved by using directional edge detection in the directions of valid shear waves as the LoG method does not provide any directional information. As shown in Figure 2.2a, the values outside the relevant wavefront are all near zero, so it's necessary to use a minimum threshold for the edge detection. A zero-crossing is identified as any two neighboring pixels with opposite sign, the threshold is applied to the difference between the two values, which represent the slope.

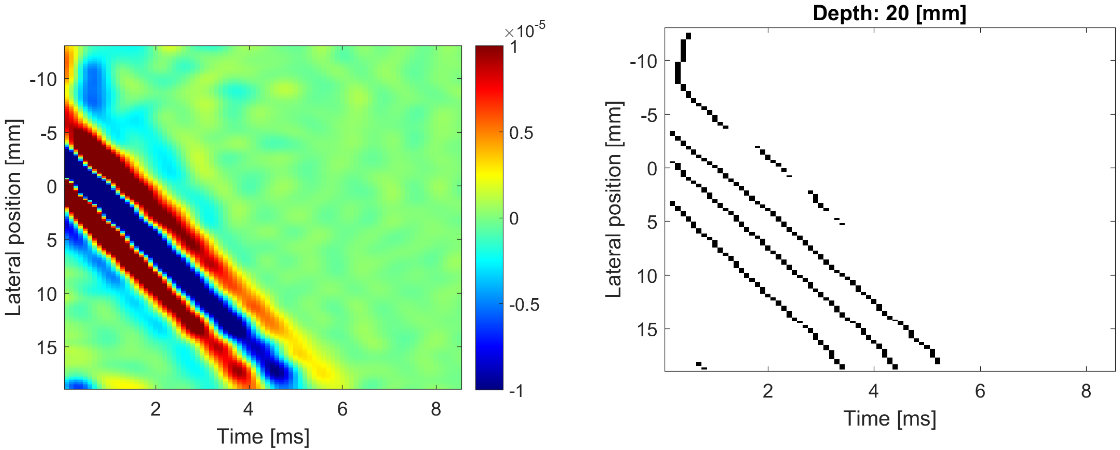

(a) After LoG-convolution.

(b) Detected edges based on a LoG-filter method

A more simple way of doing edge detection, would be to simply take the maximum value for each point in lateral direction. This has the benefit of identifying only one line, but might be inaccurate when the wavefront is wide. If the medium is homogeneous, the velocity can be found by linear regression of these maxima, but extra care must be taken to deal with outliers that are outside the area of the wave propagation or caused by noise [23].

After the edges have been detected as shown in Figure 2.2b, a Hough Transform (HT) [35], [36] is applied on the binary edge image. The HT is performed by mapping pixels to lines, for each line the edge pixels it passes through are summed, high line correlation will be seen as high values in the Hough domain. This can be seen in Figure 2.4 where each line is given by polar coordinates that are normal to the line. ρ is the distance from the origin (at the center of the image) and to the line, while θ is the angle normal to the line as shown in Figure 2.3. This relation between a standard x-y plane in cartesian coordinates and the ρ-θ plane is given by:

$$\rho = x \cos\theta + y \sin\theta \tag{2.19}$$

The figure clearly shows the three clearest lines as three points representing lines with nearly the same angle, but at different distances from the origin. It's also clear that it can be difficult to find the optimal line, as there are several good correlations for slight variations in distance and angle. In the example demonstrated, the angle in Hough domain is directly proportional to the shear wave velocity, which means that we can filter for relevant velocities by limiting the range of angles during HT, effectively cropping the resulting Hough domain.

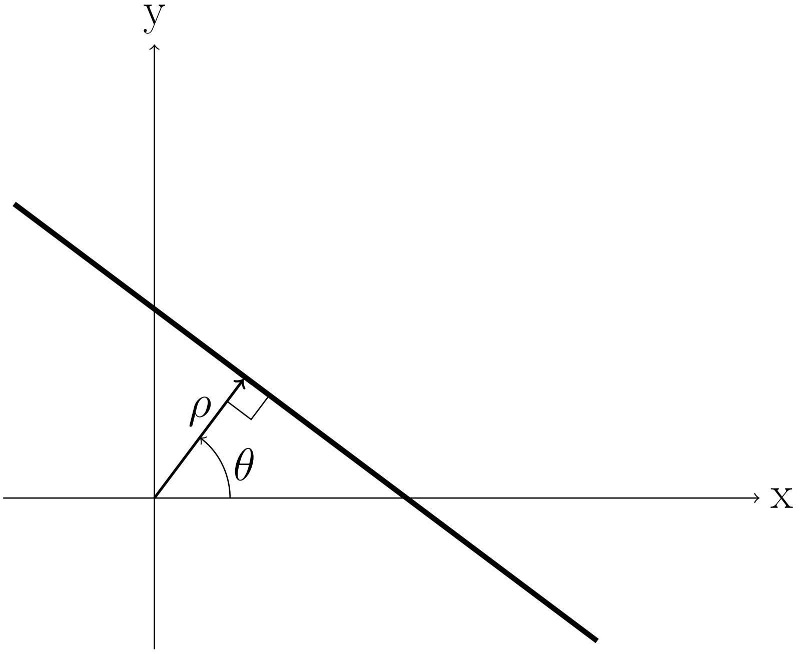

Figure 2.3: Use of polar coordinates to represent lines in Hough domain.

The lines can be found from the HT by selecting the points with the most power, which corresponds to the most probable lines. In order to identify multiple lines, it's necessary to find a reasonable lower threshold for what should be considered a line, this could be relative to the maximum power of the HT. It's also reasonable to set a minimum threshold for similarity between lines, as we can see, the HT contains several nearly identical lines with high probability. These can be avoided by setting the power of neighboring points to zero in an area around each selected point.

The lines from the HT do not have defined end points, after the lines have been selected, it's necessary to find their positions as line segments. This is necessary to get spatial information about the corresponding velocities. A way of finding these line segments is to identify and sort all the detected edge pixels along a valid line, and then group them together into line segments based on thresholds for maximum distance between points on the same line, and minimum length for a valid line.

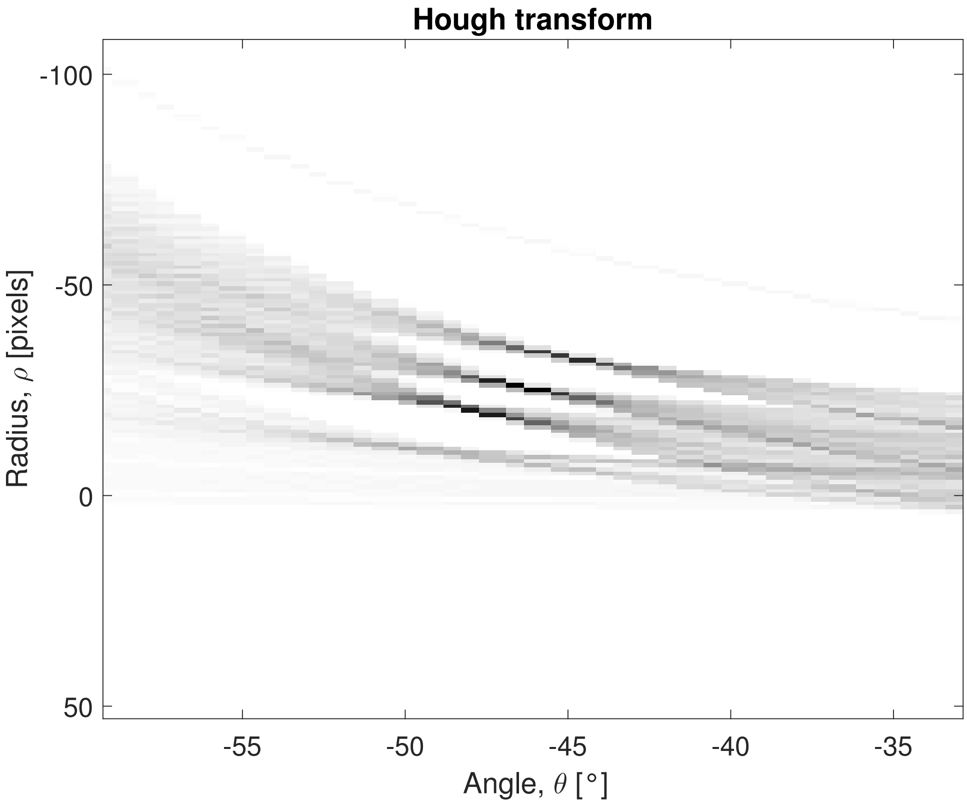

Figure 2.4: Hough transform of the binary image in Figure 2.2b. The figure is cropped to focus on the interesting area.

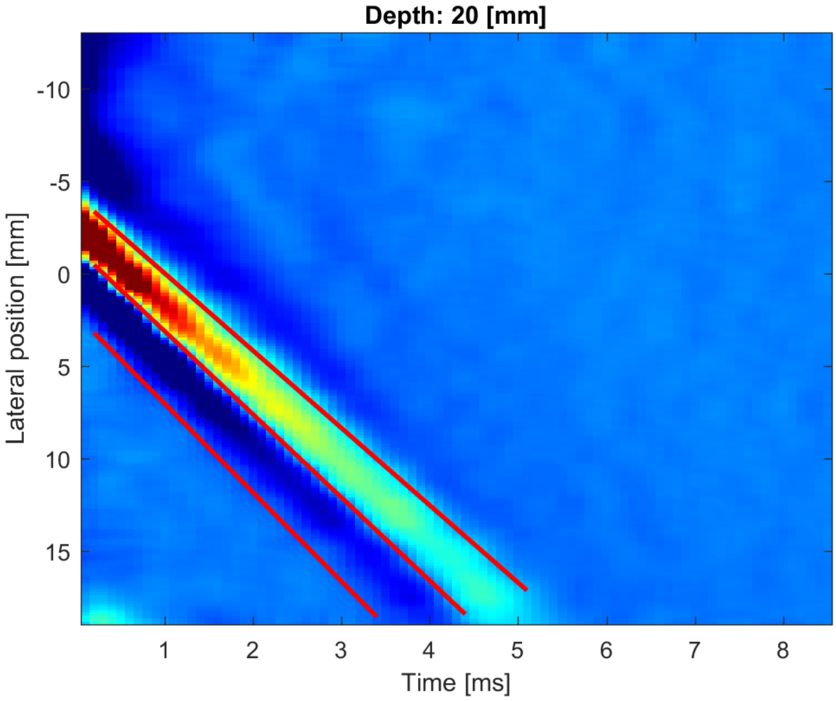

Figure 2.5: Tissue velocity map, showing shear wave propagation in the x-t plane with lines detected through HT in red.

Figure 2.5 shows the detected line segments on the TDI map. Finally, the velocity for each lateral position can be found based on the slope of the line segment passing through that position. Often there will be multiple lines at the same lateral position, then the velocities can be averaged. Combining the velocity estimates for all depths and applying some smoothing will give shear wave velocity estimates as shown in Figure 4.4e and 4.4f.

2.3.4 Cross-correlation method

Cross-correlation is a mathematical operation which gives a measure of similarity between two signals for all time delays. For two similar signals, the time delay is given by the delay, τ, of the maximum of the cross-correlation function, $r_{xy}(\tau)$ as shown in (2.20) where $x(t)$ and $y(t)$ represents two signals.

$$r_{xy}(\tau) = \sum_{t=-N}^{N} x(t)y(t+\tau) \tag{2.20}$$

A special case of cross-correlation is when the function operates on a single signal ($x(t) = y(t)$), this is called auto-correlation and is used as part of the TDI processing as seen in (2.15). As shown in section 2.3.2, TDI can be used to map the movement of the shear waves over time. The TDI values for each lateral position will correlate well with neighboring positions, with a delay corresponding to the shear wave velocity. (2.21) Shows the cross-correlation operation on the TDI values and how it's used to find the shear wave velocity in (2.22).

$$r_{\text{TDI}}(\tau) = \sum_{t=-N}^{N} TDI\left(x - \frac{N_{\Delta x}}{2}, z, t\right) \cdot TDI\left(x + \frac{N_{\Delta x}}{2}, z, t+\tau\right) \tag{2.21}$$

$$v_{shear}(x, z) = \frac{N_{\Delta x}}{\arg\max\limits_{\tau}[r_{\text{TDI}}(\tau)]} \cdot \frac{\Delta x}{\Delta t} \tag{2.22}$$

$r_{\text{TDI}}(\tau)$ represents the cross-correlation function, x and z are lateral position and depth, respectively. $N_{\Delta x}$ is the distance between the two correlated signals in lateral direction. The change between subsequent lines in the lateral direction is often very small which makes it hard to estimate velocity with a good resolution. Finding a suitable size for $N_{\Delta x}$ which is small enough to offer good lateral resolution while also being large enough to accurately estimate velocity is important. The practical cross-correlation is discrete, $N_{\Delta x}$ and τ represents pixel displacements, in order to get the corresponding velocity in meters per second we need the factors Δx, meters per pixel, and Δt, seconds per pixel. The length of the signal segments correlated are given by $2N - 1$ and can be chosen to be short to reduce the impact of noise on the valid segments containing the shear wave. If the segments are long (possibly the entire signal in time), they might be guaranteed to contain the shear wave and the process of identifying which estimates are relevant would be very simplified.

The velocity estimation can also be improved through subpixel estimation of the time delay τ_{max}. A three-point Gaussian estimator is a simple and computationally efficient subpixel estimator. The accuracy of the estimator depends on how well the shape around the peak approximates a Gaussian shape [37]. Equation (2.24) shows the three-point Gaussian estimator where τ_{max} is the integer lag corresponding to maximum correlation, while $\tau_{sub,max}$ is the position after subpixel estimation.

$$\tau_{max} = \arg\max_{\tau}[r_{\text{TDI}}(\tau)] \tag{2.23}$$

$$\tau_{sub,max} = \tau_{max} - 0.5\frac{\ln(r_{\text{TDI}}(\tau_{max}+1)) - \ln(r_{\text{TDI}}(\tau_{max}-1))}{\ln(r_{\text{TDI}}(\tau_{max}+1)) - 2\ln(r_{\text{TDI}}(\tau_{max})) + \ln(r_{\text{TDI}}(\tau_{max}-1))} \tag{2.24}$$

2.4 Dual transducers

Being able to both excite and image shear waves with a single transducer is a major advantage of ARFI/SSI techniques in terms of accessibility and ease of use. However, the shear waves are only imaged in a single fixed plane, and it’s not capable of providing information on the propagation in other directions or over long distances. By using two transducers, one to excite the shear waves and the other for imaging, it’s possible gather more information about the attenuation of shear waves over longer distances, as well as the propagation in elevation direction. Another important aspect of a dual transducer setup is that it’s possible to image shear waves in inaccessible areas, where it’s hard to excite shear waves outside of the ROI with a single transducer.

Dual transducer setups have been used for both conventional US [38] and SWE with techniques like *shear wave dispersion ultrasound vibrometry* (SDUV), which uses a continous ultrasound beam at a focal point (it does not generate a 2D estimate) [10]. For transient elastography techniques however, there are no known implementations of a dual transducer setup.

2.5 Phantom

In order to assess the properties and feasibility of SWE in a safe manner, it's necessary to use phantoms with ultrasonic properties similar to tissue. Polyvinyl alcohol (PVA) cryogel phantoms are simple to make, and the elastic properties of the phantom can easily be adjusted during production by varying the number of freeze-thaw cycles used. The process involves mixing PVA-powder with water, heating up the mixture to about 80 °C while stirring, and then cooling it down before pouring it into a mold and starting a series of "freeze-thaw cycles". One freeze-thaw cycle consists of a period of freezing temperatures, followed by a period, usually of equal length, in room temperature [39]. For elastography, the most interesting property is Young's modulus, which has been found to increase with the number of freeze-thaw cycles. This makes it possible to construct heterogeneous PVA phantoms by combining phantoms with different numbers of cycles.

There are many possible variations in the PVA phantom production, such as the temperatures used, duration of freeze and thaw periods, PVA-powder concentration and the possible addition of scatter particles. But there's also other ways of producing US phantoms, mainly hydro-gels based on agar, gelatin or a mix of both. They all have the desirable properties of a mass density and Poisson's ratio close to tissue (about $1000\,\mathrm{kg/m^3}$ and 0.5 respectively), they also have good attenuation properties and the elastic properties don't change significantly over time [40]. There are also examples of more complex methods that have been used to mimic specific heterogeneous tissue across multiple modalities, but that has not been the topic of this project [41].

Chapter 3

Methods

This chapter will describe the physical setup for the measurements, the structure and parameters of the ultrasound sequences, the post-processing techniques used and the production of the PVA phantoms.

3.1 Measurement setups

All measurements were made with a Verasonics Vantage 256 ultrasound research system (Verasonics, Kirkland, WA, USA) using one or two L11-4v transducers. The L11-4v is a linear transducer with 128 channels, all of which were used for imaging, while only 64 elements were used for the transmission of ARFI pulses. The central frequency, f_0, was 4.8 GHz for both imaging and ARFI in all measurements. The ARFI pulses had a pulse length of 100 µs and a PRF of 5 kHz, while the imaging was done with a PRF of 10 kHz and a pulse length of 0.2 µs (2 half-periods). The scripts used were modified versions of a shear wave example-script by Verasonics. The probes were fixed in a stationary position on the phantoms for all measurements, as shown in Figure 3.1 and Figure 3.2. The dual transducer setup was only used on a homogeneous PVA phantom, while the single transducer setup was used on all three phantoms (homogeneous PVA, heterogeneous PVA, and a multi-purpose phantom by CIRS). Beamformed IQ-data was provided by the Verasonics-script, it was saved, extracted and further processed offline as described in section 3.2.

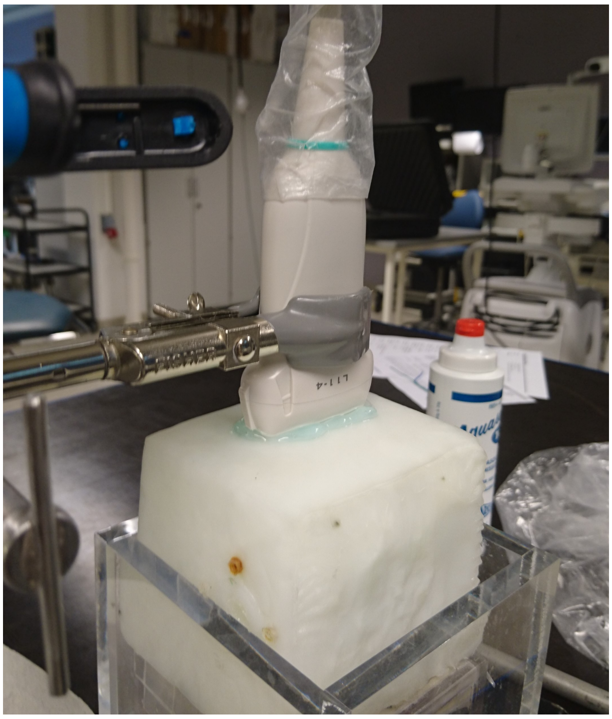

Figure 3.1: Measurement setup for a single US probe on a homogeneous medium.

3.1.1 Dual transducers

For the measurements done with two transducers, only the homogeneous phantom was used, as the heterogeneous phantom was too small to fit two US probes on the same plane. The two probes were placed at a slight angle, in a line, in order to fit both on the phantom as shown in Figure 3.2. Positioning the probes in a line meant that the estimated velocity was expected to be the nearly the same as for a single transducer, but slightly higher due to the angle. Measurements at different angles and distances between the probes would be very relevant to the assessment of this setup, but were not made because of space constraints on the phantom. With two transducers, the time it takes for the shear wave to propagate through the ROI is no longer dependent on just the velocity, but also the distance between the transducers. In order to ensure that the shear wave is properly imaged, the image acquisition time is increased for two transducers (20 ms). Additionally, they imaging-PRF was reduced to 5 kHz in order to keep the processing time on the same level as the single transducer setup.

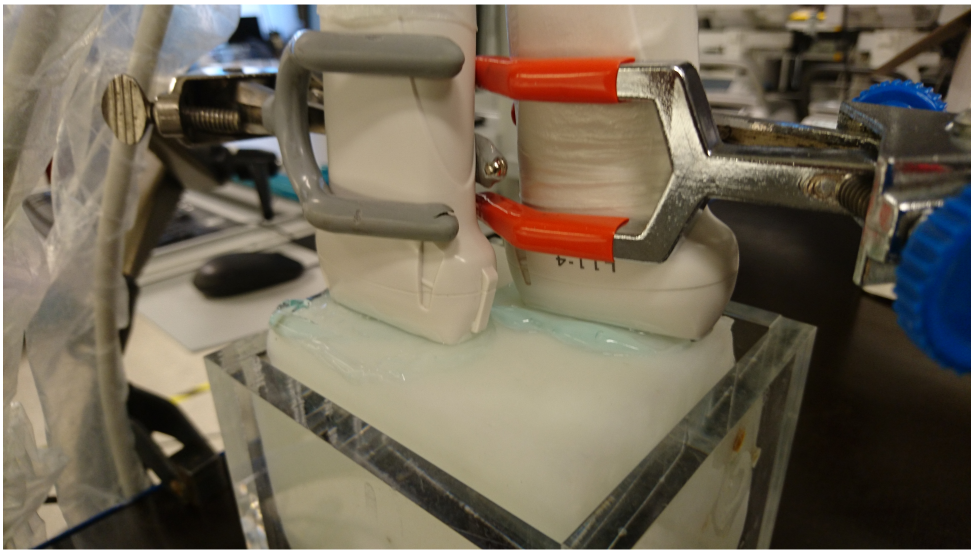

Figure 3.2: Setup for two probes on a homogeneous medium.

3.2 Processing algorithms

One of the core challenges of SWE is to accurately detect and estimate the velocity of the shear waves. In this project, two different methods with very different properties were used: a traditional approach based on cross-correlation, and an alternate method based on line detection using Hough Transform (HT) was also implemented with some success. For all processing methods, a TDI algorithm was first used on the IQ data to detect the presence of the shear waves.

The beamformed IQ-data was provided by the Verasonics system and stored for offline processing. The IQ-data had a resolution of 4 samples/λ in depth (where λ is the wavelength of speed of sound) and 2 samples/λ in lateral direction, with a ROI of $100 \times 90\,\lambda$, or 32×29 mm, or 400×180 pixels. The difference between subsequent frames was then calculated as described in equation (2.15). A spatial moving average filter was applied to remove high frequency noise before the tissue velocity was calculated as described by equation (2.17) and then low-pass filtered in time. This tissue velocity map was then turned into an acceleration map with a simplified derivation done by taking the difference between subsequent frames in order to improve the wavefront contrast further. This "TDI" map shows the shear wave propagating and is the basis for the following velocity estimation algorithms.

3.2.1 Line detection with Hough Transform

The line detection method relies on the TDI maps in the x-t plane (lateral direction and time) and estimates velocities for each depth individually. The method used is in line with the one described in section 2.3.3. A LoG-filter is applied to the TDI map, and zero-crossings steeper than a threshold are marked as an edge in a binary edge-map. An alternate method is also presented which uses the maximum amplitude of the TDI maps (in x-t plane) for each lateral position and creates a binary "edge-map" based on those positions. A Hough transform is then applied to the edge-map with an angle-range corresponding to valid velocities, in this case velocities from 0.5 to 10 m/s with a 0.1 m/s resolution. The most likely lines are represented as peaks in the HT image, the points with highest value are then selected. A maximum of 10 points is chosen as an upper limit to reduce the likelihood of spurious lines, and a lower threshold is set as a minimum of the highest value, in this case 70 %. An area around each selected point in the HT is set to 0 to ensure each point represents different lines. Line segments are then found by mapping the selected lines to the binary edge-map and the presence of edges is used to decide the end points for the line segments.

An example of lines detected in a homogeneous medium is shown in Figure 2.5.

With the line segments corresponding to the wave propagation identified, the velocity is estimated for each lateral position based on the angle of the line passing through, which is given by the HT. The velocity is estimated as shown in (3.1) where Δx and Δt represent the resolution in lateral direction and time respectively. c is the speed of sound, f_0 is the central frequency of the imaging pulses, and PRF is the imaging PRF. 90° are added to the angle because the angle in Hough domain is perpendicular to the line.

$$\begin{aligned} c_t &= \tan\left(\theta_{\mathrm{HT}} + 90^\circ\right) \frac{\Delta x}{\Delta t} = \tan\left(\theta_{\mathrm{HT}} + 90^\circ\right) \frac{\lambda/2}{1/PRF} \\ &= \tan\left(\theta_{\mathrm{HT}} + 90^\circ\right) \frac{cPRF}{4f_0} \end{aligned} \tag{3.1}$$

In most cases, more than one line will pass through a lateral position, in those situations the velocities for all lines passing through a lateral position are averaged. This process is repeated for all depths (400 times for the current ROI), and a Gaussian averaging filter is applied to smooth the resulting shear wave velocity map.

3.2.2 Cross-correlation

Just like the line detection method, the cross-correlation method uses the TDI-processed maps in the x-t plane as a basis. For each lateral position, a line segment (in time) is selected and correlated with the corresponding line segment at a different lateral position. All of the results presented here are based on a lateral difference of 4 mm, or 25 pixels between the two line segments in order to get more reliable, noise-resilient results. The lag corresponding to the maximum correlation coefficient is found and adjusted with a three-point Gaussian subpixel estimator. The lag and the correlation coefficient is saved, considered to be localized halfway between the two lines in lateral direction, and in the middle of the line segment in time.

Two main versions of this cross-correlation method were used, one which uses the full length of the TDI signal in time (which will be known in this text as "full-width"). The other uses shorter segments in order to reduce the impact of noise and artifacts on the most relevant segments. When using shorter segments, it's necessary to iterate over the range of data with slightly different time ranges for each segment to ensure the shear wave is covered, this means that there's multiple correlation lags estimated for each lateral position. In order to avoid the values estimated with noise segments, a minimum threshold for the correlation coefficient is used. The lags corresponding to correlation coefficients above the threshold are averaged. For the method with shorter segments, each segment was 40 pixels long, or 4 ms with a PRF of 10 kHz.

The cross-correlations are iterated over the TDI map in both time and lateral direction for each depth. A threshold is then set as 1 % of the highest correlation coefficent, values below the threshold are discarded. The lags corresponding to velocities beyond the valid range are also discarded at this point If there are other valid values for the same lateral position, the poor estimates are merely omitted from the average lag. In areas where all values are discarded, there are no velocity estimates either.

The process is repeated for every depth (each pixel) to create a full spatial 2D map of the shear wave velocities. Finally the shear wave velocity map is smoothed using a Gaussian filter, in this case the filter is 15×15 pixels large and with a standard deviation σ of 10 pixels, or $1.2\,\mathrm{mm} \times 2.4\,\mathrm{mm}$ large with $\sigma_x = 1.6\,\mathrm{mm}$ and $\sigma_z = 0.8\,\mathrm{mm}$. The smoothing filter also interpolates over regions without valid values.

Cross-correlation with line detection

While using a minimum treshold for correlation coefficients helps in filtering out noise, it may not be sufficiently selective in choosing the best estimates. Another method is used which combines the velocity estimates from the cross-correlation method with the line detection method. The cross-correlation method is used as described in the previous section with smaller time segments, creating a velocity/lag estimation map corresponding to the TDI map in the x-t plane. Line detection based on edge detection and Hough transform is also done, as described in section 3.2.1, but instead of using the slope of the lines to estimate velocity, the lines are used to select the valid cross-correlation estimates.

3.3 Phantoms

Three different US phantoms were used in this project: a homogeneous PVA phantom, a heterogeneous PVA phantom, and a multi-purpose multi-tissue phantom model 040GSE, by CIRS (Computerized Imaging Reference Systems Inc, Norfolk, VA, USA). The homogeneous PVA phantom was produced before the start of this project, and the exact details regarding the phantom production is unknown, but it's reasonable to assume that the general method is the same as for the heterogeneous phantom. The heterogeneous phantom was produced by mixing 90 % water and 10 % PVA powder while stirring in a glass container. The container was then sealed with aluminium foil to avoid dehydration, and put into a water bath with shaking functionality to ensure even heating of the liquid, as shown in Figure 3.3. The water bath was heated to 80 °C and an external thermometer was put into PVA liquid to ensure correct temperature. After the PVA liquid had reached 80 °C, it was removed from the water bath and set to cool down by the ambient room temperature of ~24 °C while being stirred by a magnetic stirrer. After the liquid reached 40 °C it was poured into two plastic molds, one rectangular with a cylindrical protrusion, and another cylindrical mold corresponding to the protrusion. Figure 3.4 shows the larger rectangular mold. The phantoms were cooled down further to 30 °C before they were put in a freezer to start the freeze-thaw process.

Figure 3.3: The PVA mixture in the water bath during the heating process. The bath was covered with a lid during this process.

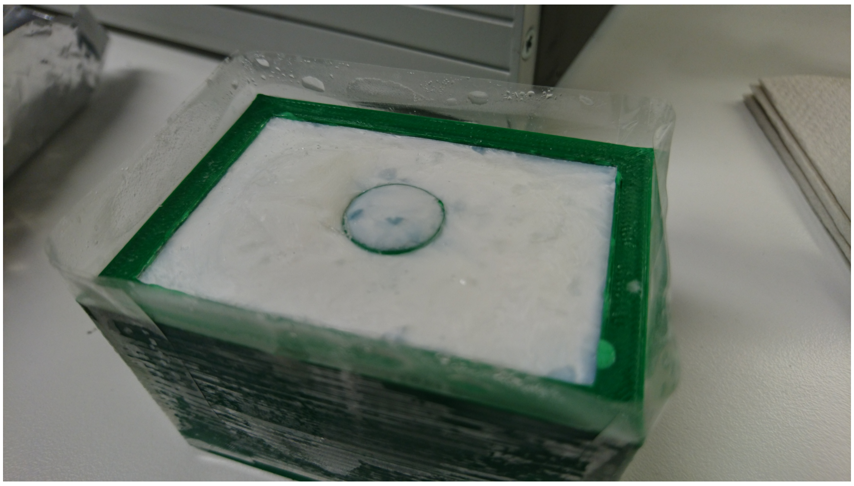

Figure 3.4: Part of the heterogeneous phantom, directly after a freeze process.

The freeze-thaw cycles consisted of 24 hours of freezing (−18 °C), followed by 24 hours of thawing in room temperature ~24 °C. The large phantom went through 3 freeze-thaw cycles, while the small cylindrical "cyst" had 5 cycles in order to get a stiffer cyst. After production and while they were not being used, the phantoms were stored in a refrigerator at 4 °C. The two parts of the phantom were put together and imaged, but the interface between the two parts caused strong reflections and we were unable to propagate shear waves through the cyst. The phantom was submerged in water, gaps filled with transmission gel, and finally put through an additional freeze-thaw cycle to improve the coupling, but none of the attempts were successful. Instead, a new batch of PVA liquid was prepared with the same method, the two phantom parts were separated and put into larger containers, and these containers were filled with the PVA liquid immediately after cooling down to 30 °C. The new phantoms went through two freeze-thaw cycles, which means the rectangular part of the phantom had now been through 6 cycles in total. After this process, both regions could be imaged successfully.

Even though the production process was the same both times, the second PVA batch was considerably larger, and there were some issues with keeping the PVA mixture homogeneous during the heating process. As a result this mixture had particles in it that might impact the homogeneity of the phantom. While not immediately obvious, the particles can be seen in Figure 3.5.

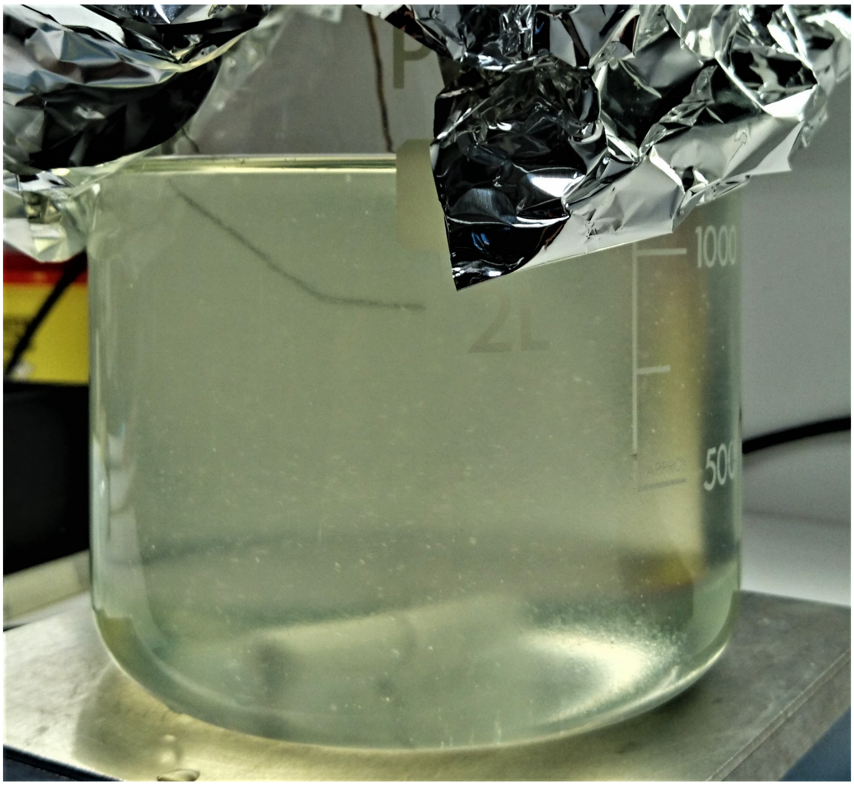

Figure 3.5: Some particles that were not fully dissolved in the PVA mixture can be seen.

Figure 3.6: The second mold with the first rectangular PVA phantom, before adding more PVA mixture.

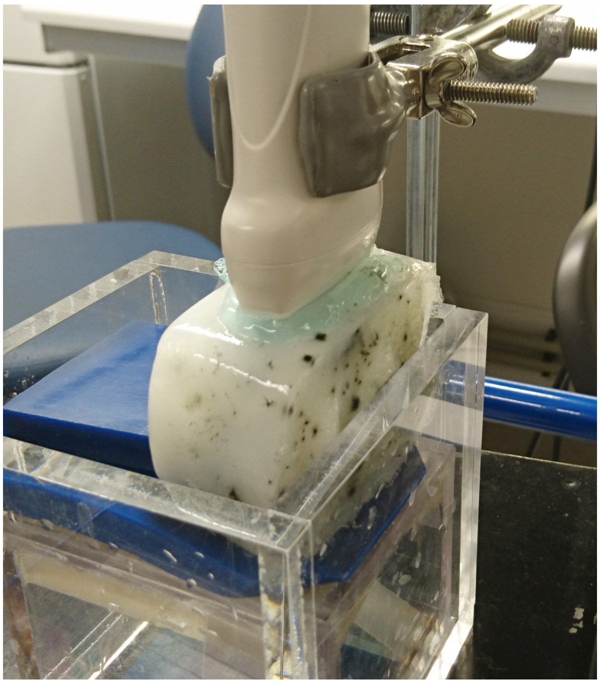

Figure 3.7: The finished heterogeneous phantom during measurements. The picture is taken a while after it was finished and had considerable bacterial growth.

3.4 Thermal measurements

The thermal measurements are made with a thermocouple data logger, model: USB TC-08, by Pico Technology (Pico Technology, St. Neots, Cambridgeshire, UK), connected to a computer running Matlab, which in this case is the same Verasonics system connected to the US probe. The thermal sensors are "cement-on surface-mount" thermocouples by Omega (Omega Engineering, Stamford, Connecticut, USA), model CO1-K used on the transducer. Only a small set of thermal measurements are made considering it is not the main focus of the project, but is still important to the safety of the transducer and patients. The single transducer setup is used, with an SSI sequence of 5 ARF pulses centered at 25 mm depth with 5 mm intervals for all measurements. The thermal sensor is placed on the transducer, on the side that is also used to transmit ARF pulses in order to ensure the temperature measured is the highest temperature generated. A second thermal sensor is used to measure the ambient temperature and to ensure that the measurements are not significantly impacted by external sources. Because the temperature takes a long time to reach ambient temperature after a temperature rise, new measurements are started as long as the surface temperature on the transducer is within 1 °C of the ambient temperature.

Chapter 4

Results

This chapter will present the experimental results obtained through the methods described in Chapter 3. It's possible to make reasonable shear wave velocity estimates "manually" from the TDI-maps, but "true" tissue stiffness is unknown for all measurements except for the cysts in the multi-purpose phantom. As a result, the shear wave velocities are presented directly for most measurements, rather than the Young's modulus which they are an estimator for. With the expectation that the relation between shear wave velocity and Young's modulus is simple and given by equation (2.6). In order to simplify comparisons in this chapter, all the shear wave velocity maps presented are based on velocity ranges that are fixed for measurements of the same medium, but might otherwise differ (i.e. between homogeneous and heterogeneous phantoms).

4.1 Wavefront

The propagation of the shear wave through a homogeneous phantom is shown in Figure 4.1. A single ARF pulse, as seen in Figures 4.1a-c, covers a very limited range in depth initially, but it propagates with a spherical wavefront which covers a greater range in depth as it travels in lateral direction. When transmitting an SSI sequence, e.g. 5 ARF pulses with 5 mm intervals as shown in Figures 4.1d-f, the wavefront becomes nearly plane and covers a greater area. The plane wavefront is caused by constructive interference of the individual shear waves from the ARF pulses, but if the intervals between the shear wave sources are too great, the interference will not be sufficient to create a plane wave as seen in Figures 4.1g-i where 2 ARF pulses are transmitted with a 20 mm interval.

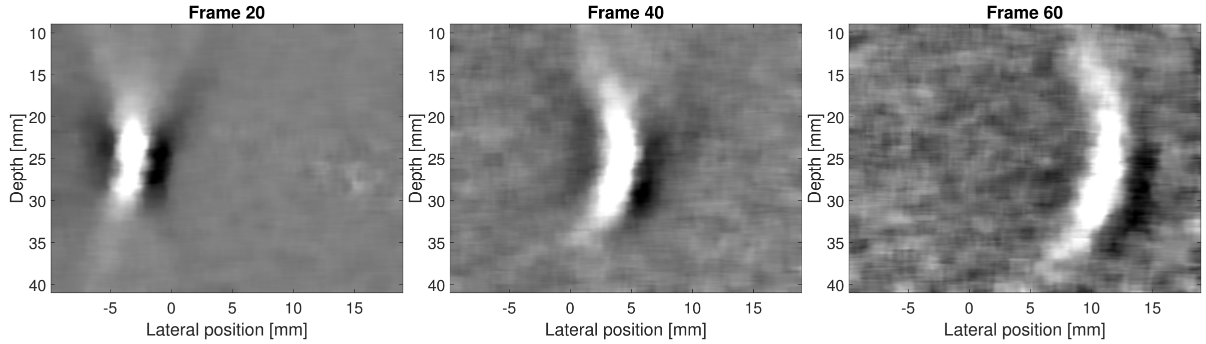

(a) 1 push, frame 20 (b) 1 push, frame 40 (c) 1 push, frame 60

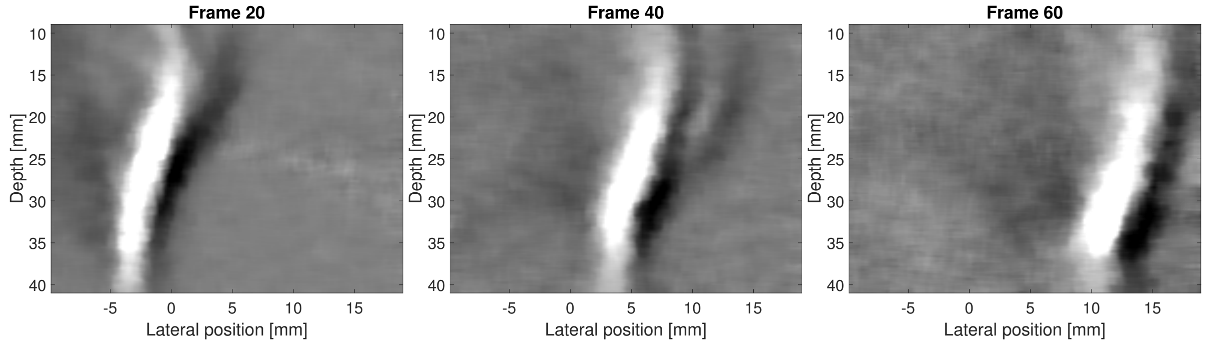

(d) 5 pushes, 5 mm intervals, frame 20 (e) 5 pushes, 5 mm intervals, frame 40 (f) 5 pushes, 5 mm intervals, frame 60

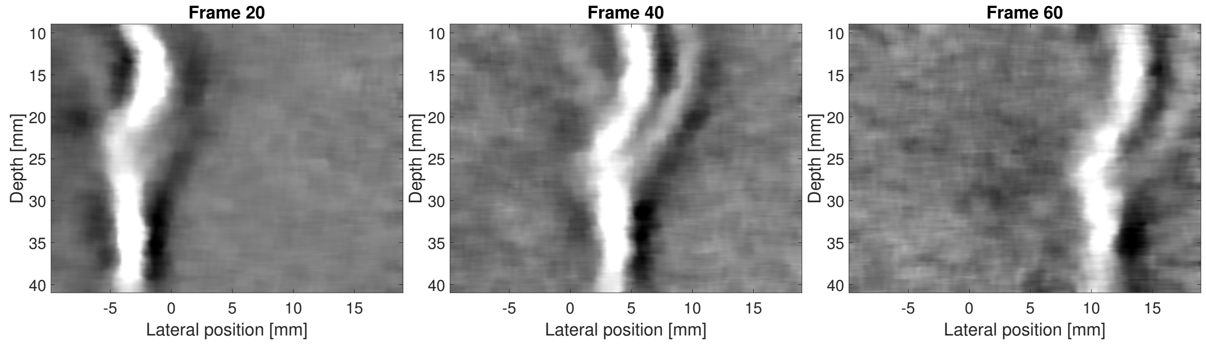

(g) 2 pushes, 20 mm interval, frame 20 (h) 2 pushes, 20 mm interval, frame 40 (i) 2 pushes, 20 mm interval, frame 60

Figure 4.1: Tissue velocity maps after TDI processing, showing the shape of the wavefront and how it propagates in a homogeneous medium over time.

The wave propagagations showed in Figure 4.1 are based on tissue velocity maps with normalized amplitude for each figure. This is particularly clear in Figure 4.1c where the background noise is far more prominent as a result of the relatively low signal power with a single ARF pulse. The amplitude of the different sequences are better compared in Figure 4.2 where all the figures are based on the same tissue velocity range. It's clear that a single ARF pulse has a lower signal power than the SSI equivalents, and transmitting two ARF pulses too far apart as shown in Figure 4.2c does not generate sufficient constructive interference to improve the power. On the other hand, Figure 4.2b shows two ARF pulses focused very close to each other (1 mm) which keeps the curved wavefront of the single ARF pulse, but greatly improves the amplitude of the shear wave. Two SSI sequences with 5 mm intervals are also shown, they both have a similar plane wavefront, but Figure 4.2e uses more ARF pulses and as a result covers a greater range in depth. Figure 4.2f is based on 10 ARF pulses transmitted with 2 mm intervals and shows a strong wavefront, but the wavefront is also wider as a result of the short intervals between ARF pulses.

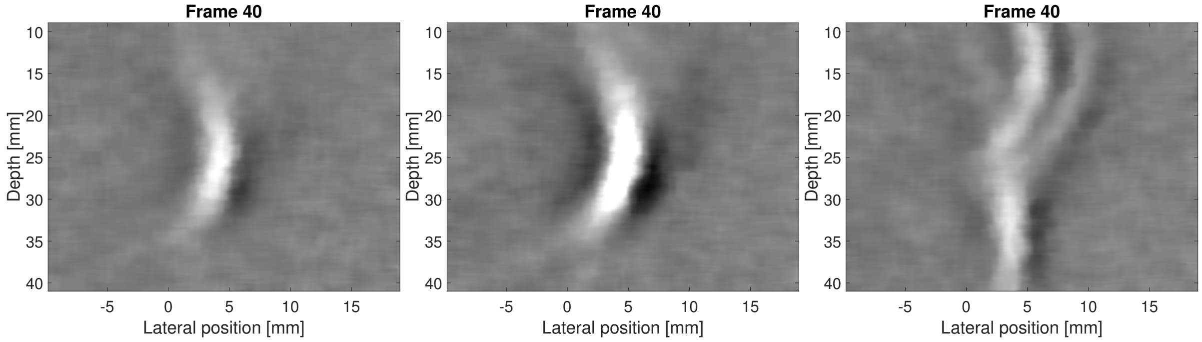

(a) 1 push (b) 2 pushes, 1 mm intervals (c) 2 pushes, 20 mm intervals

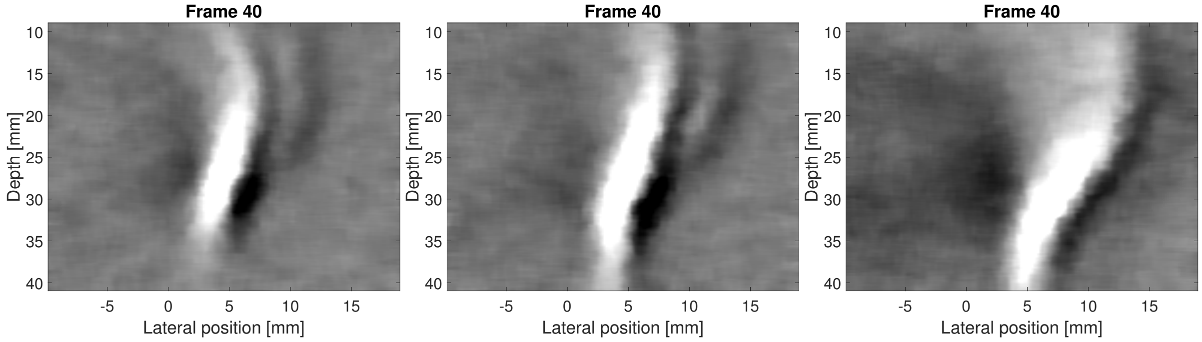

(d) 3 pushes, 5 mm intervals (e) 5 pushes, 5 mm intervals (f) 10 pushes, 2 mm intervals

Figure 4.2: Tissue velocity maps after TDI processing, scaled to the same amplitude. All the individual figures are based on the frame at the same time after the last push of the SSI sequence. Using a homogeneous phantom.

4.2 Velocity estimator

In order to assess the accuracy and reliability of the different velocity estimation techniques, Figure 4.4 shows the velocity estimates for a homogeneous medium with both a single ARF pulse, and an SSI sequence with 5 ARF pulses. The single ARF pulse is focused at 25 mm depth, and the SSI sequence is centered at 25 mm with 5 mm intervals. We can see that the cross-correlation method has a lot more local variation than the line detection method, which is to be expected due to the higher resolution of the cross-correlation method. It's also clear that the SSI sequence is capable of covering a larger area, the areas without any data in the cross-correlation estimates have been removed by applying a threshold for minimum power of the cross-correlation coefficients. Combining cross-correlation with line detection for selection of relevant estimates improves the valid estimates, but the area considered valid is smaller. Which is a reasonable approach considering a significant portion of the velocity estimates outside of that scope are greatly overestimated by the other methods. Using line detection with maximum amplitude from the tissue velocity map rather than the edge detection appears to provide smoother estimates, and provide them over a larger region. The last method presented is the full-width cross-correlation method which offers smooth velocity estimates similar to the ones provided by the cross-correlation with line detection method. It does however, also provide estimates in a larger region (with the caveat that it's more error prone in the selection of valid estimates.)

The average of multiple measurements is shown in Figure 4.5 where 10 individual measurements are combined. The difference between these averaged velocity maps and the individual velocity maps is tiny, which is reflected in the standard deviation estimate. Figure 4.6 shows the standard deviation for each individual pixel calculated from 10 samples with the same settings. In general, the standard deviation is low, typically $<0.1\,\mathrm{m/s}$ except for the edges.

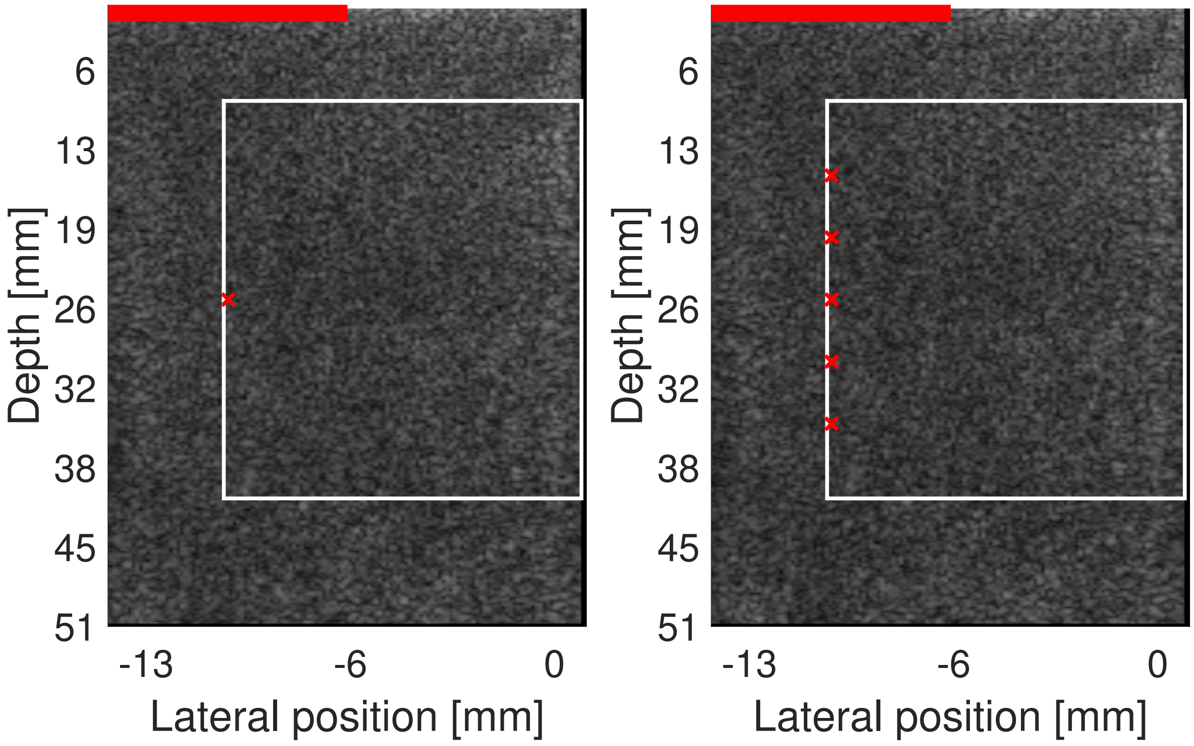

(a) 1 push

(b) 5 pushes

Figure 4.3: B-mode image of the homogeneous phantom. The red crosses indicate the positions of the ARF pulses. The white rectangle indicates the ROI used to estimate shear wave velocity.

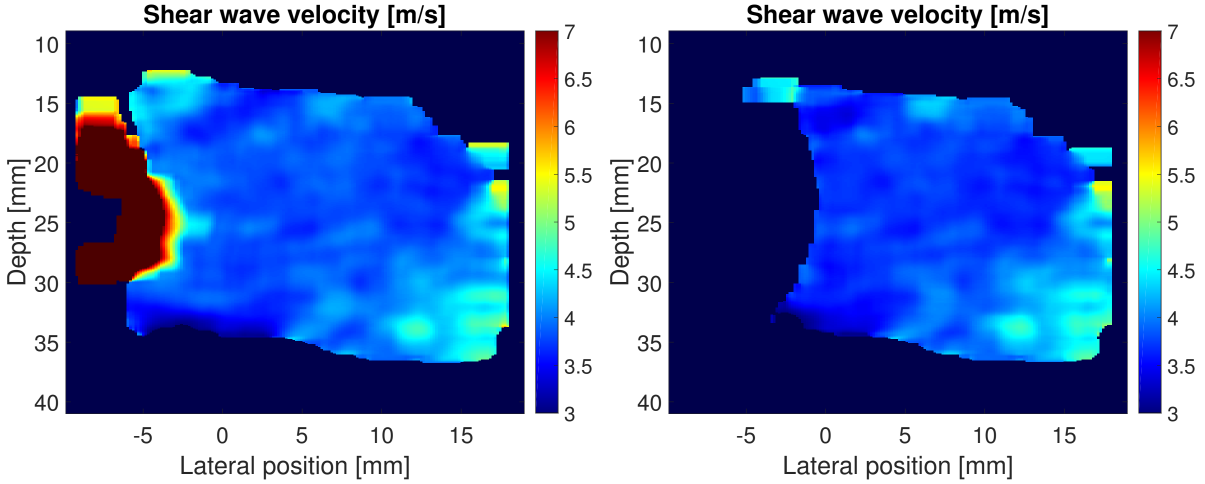

(a) 1 push, cross-correlation

(b) 1 push, cross-correlation + line detection

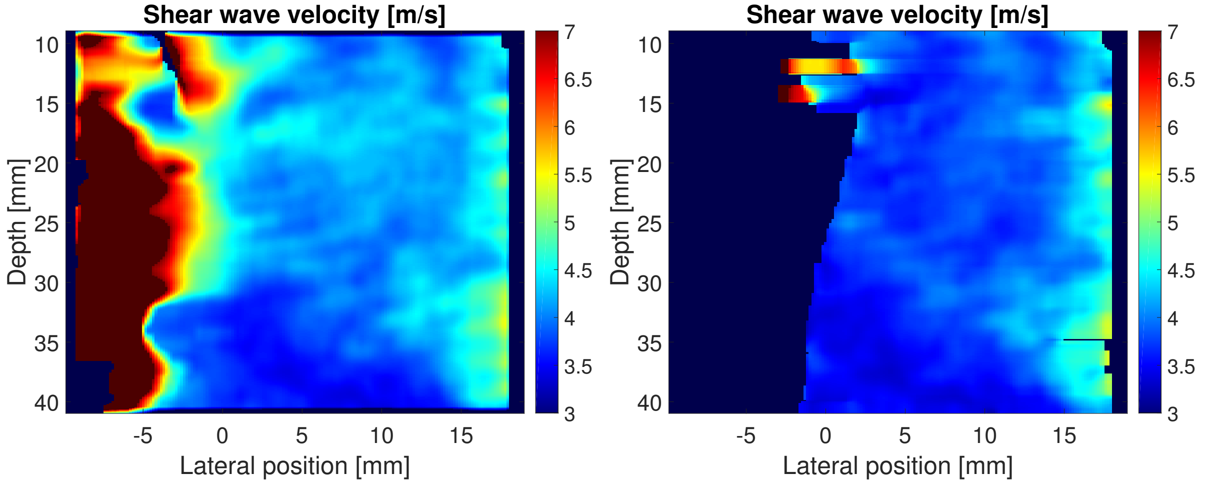

(c) 5 pushes, cross-correlation

(d) 5 pushes, cross-correlation + line detection

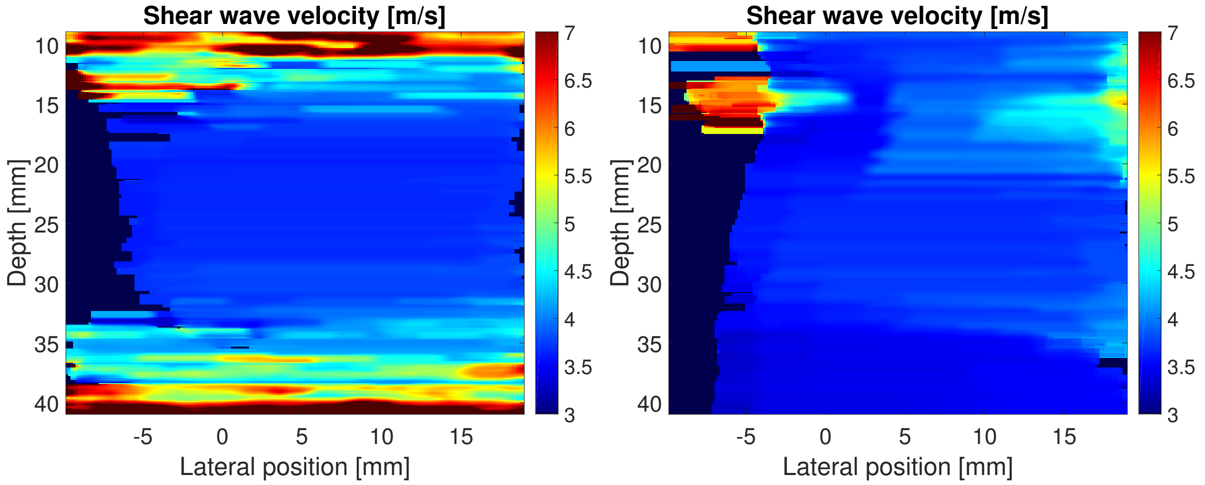

(e) 1 push, line detection

(f) 5 pushes, line detection

Figure 4.4: Velocity map with different post-processing techniques. All have focus centered at 25 mm depth.

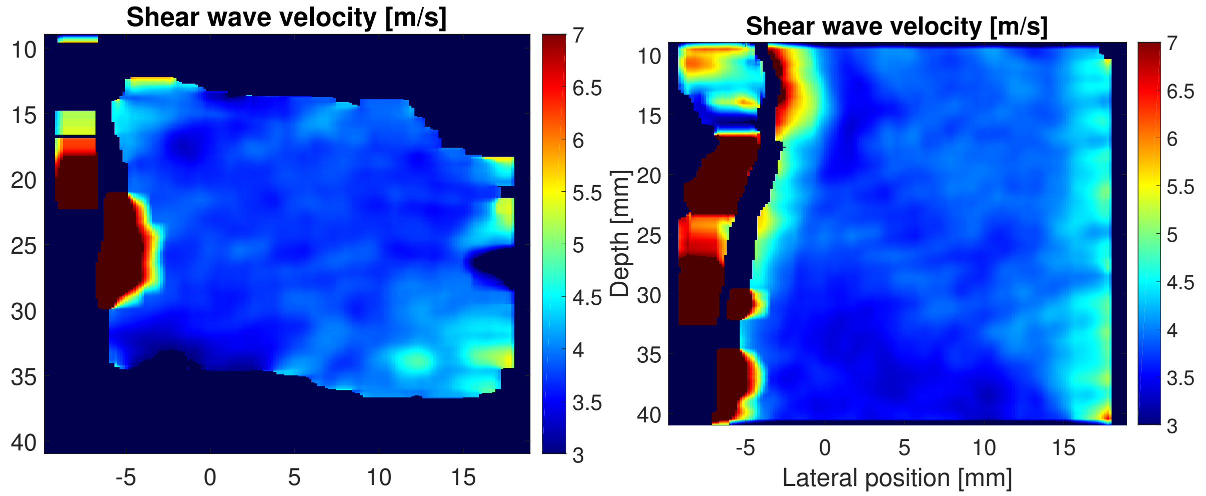

(g) 1 push, full-width cross-correlation

(h) 5 pushes, full-width cross-correlation.

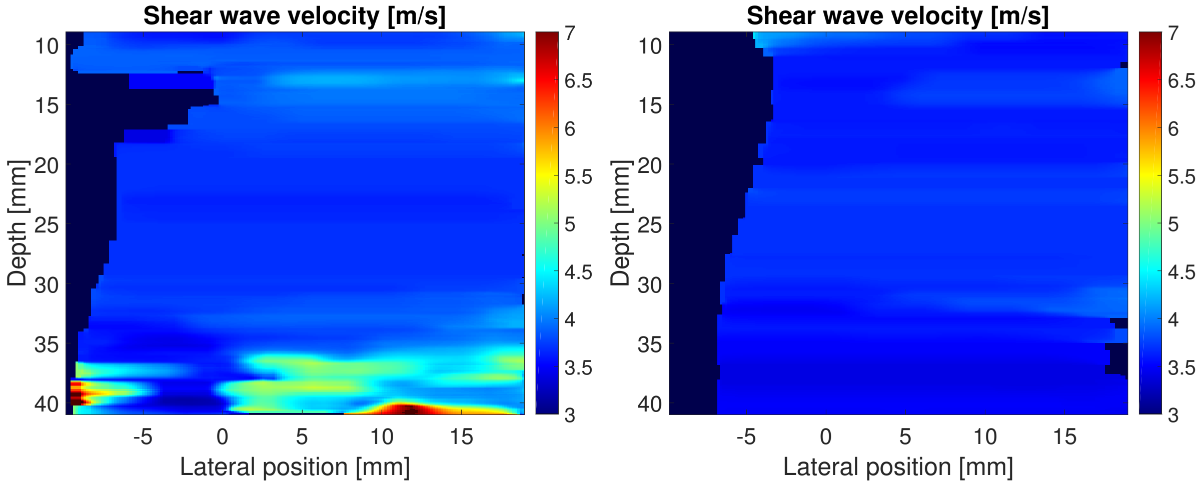

(i) 1 push, line detection with maximum amplitude.

(j) 5 pushes, line detection with maximum amplitude.

Figure 4.4: Velocity map with different post-processing techniques. All have focus centered at 25 mm depth. (cont.)

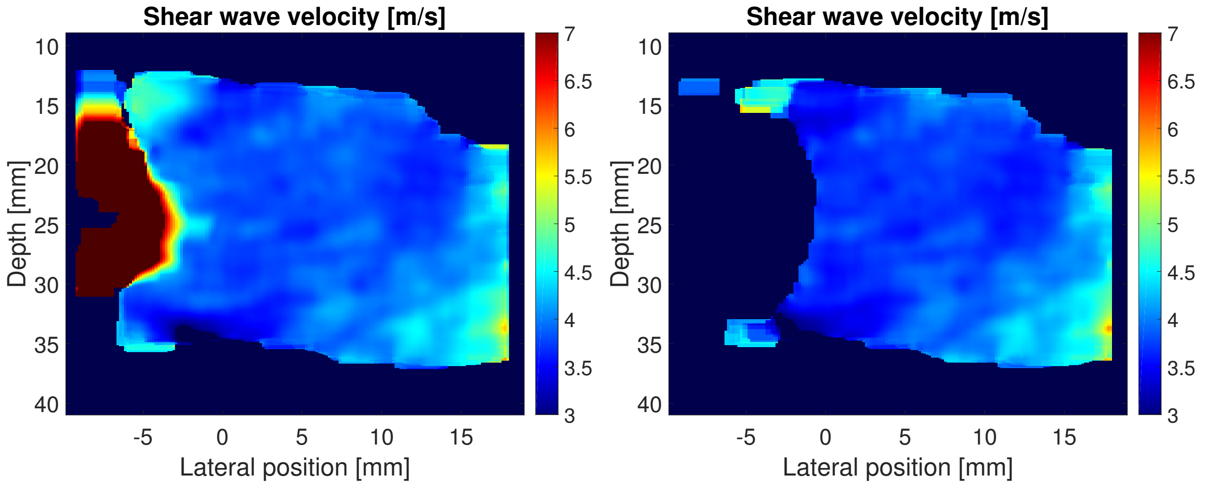

(a) 1 push, cross-correlation, avg. of 10 frames.

(b) 1 push, cross-correlation + line detection, avg. of 10 frames.

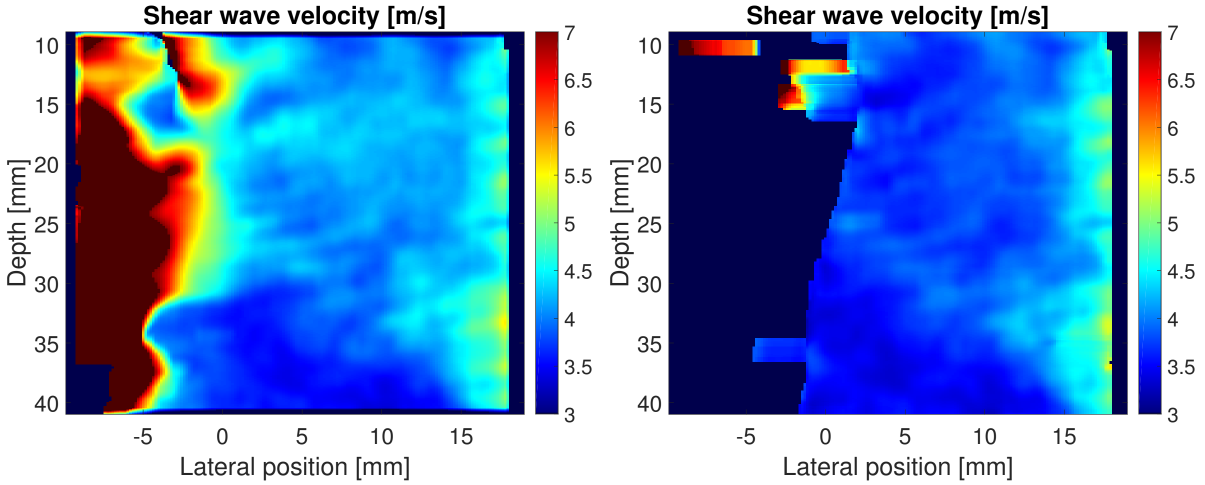

(c) 5 pushes, cross-correlation, avg. of 10 frames.

(d) 5 pushes, cross-correlation + line detection, avg. of 10 frames.

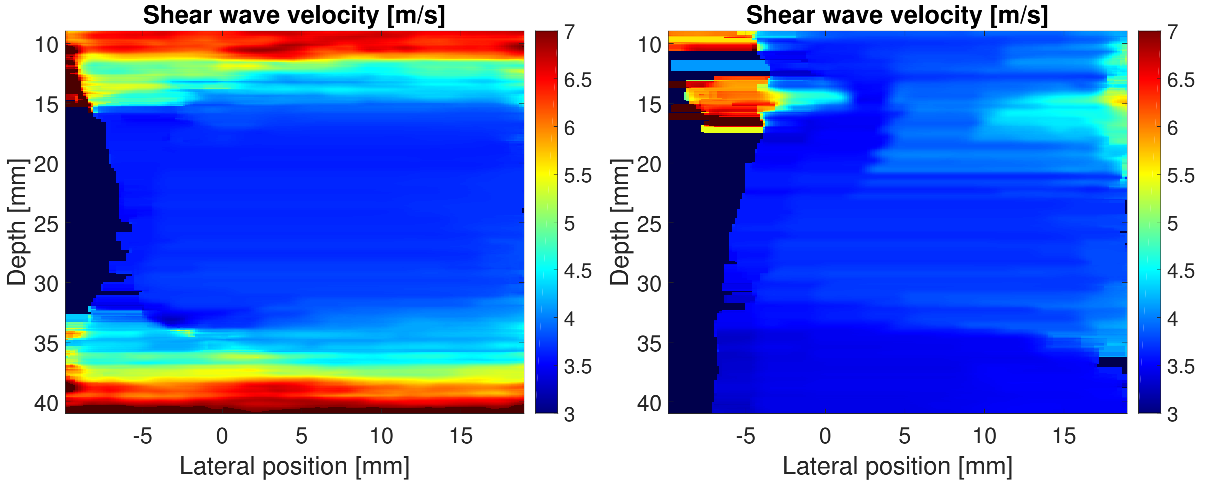

(e) 1 push, line detection, avg. of 10 frames.

(f) 5 pushes, line detection, avg. of 10 frames.

Figure 4.5: Time-averaged velocity maps of 10 frames each, corresponding to the same measurements as in Figure 4.4.

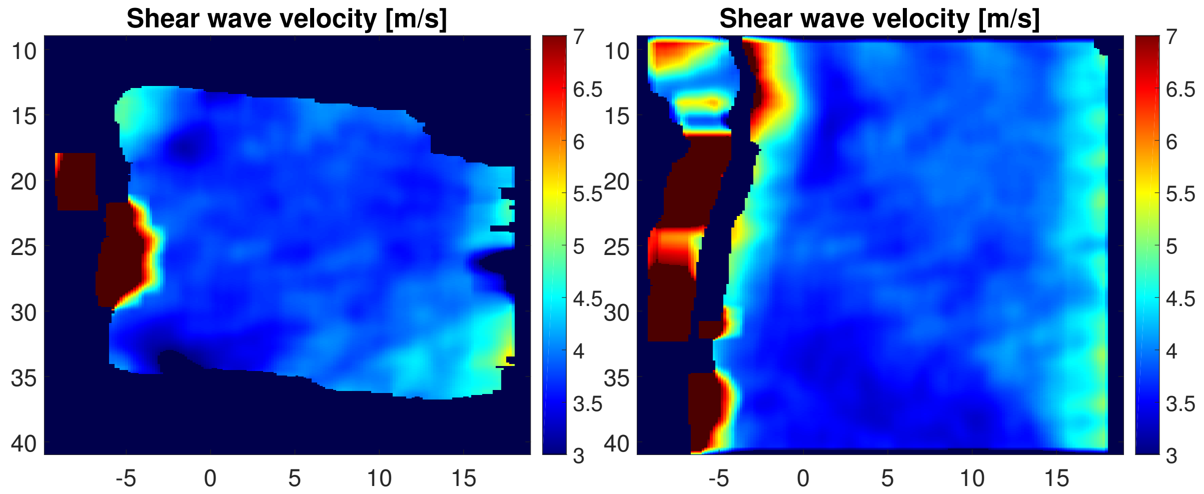

(g) 1 push, Full-width cross-correlation, avg. of 10 frames.

(h) 5 pushes, Full-width cross-correlation, avg. of 10 frames.

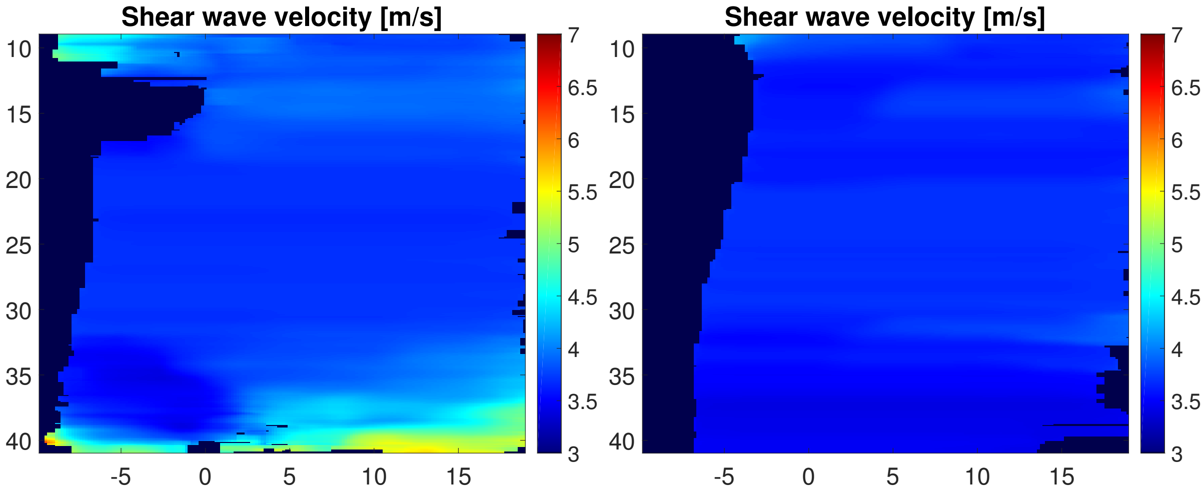

(i) 1 push, line detection with maximum amplitude, avg. of 10 frames.

(j) 5 pushes, line detection with maximum amplitude, avg. of 10 frames.

Figure 4.5: Time-averaged velocity maps of 10 frames each, corresponding to the same measurements as in Figure 4.4. (cont.)

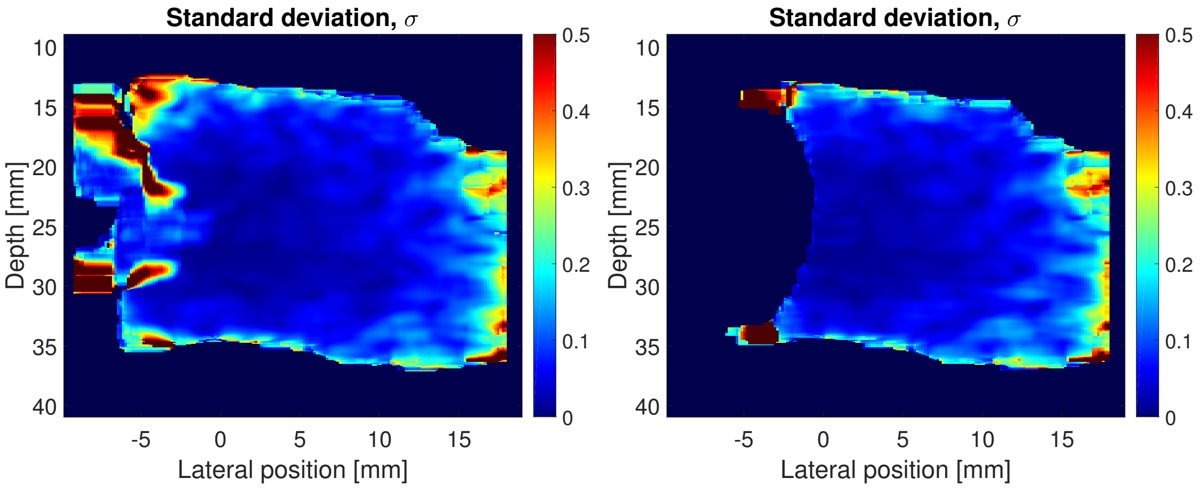

(a) 1 push, cross-correlation

(b) 1 push, cross-correlation + line detection

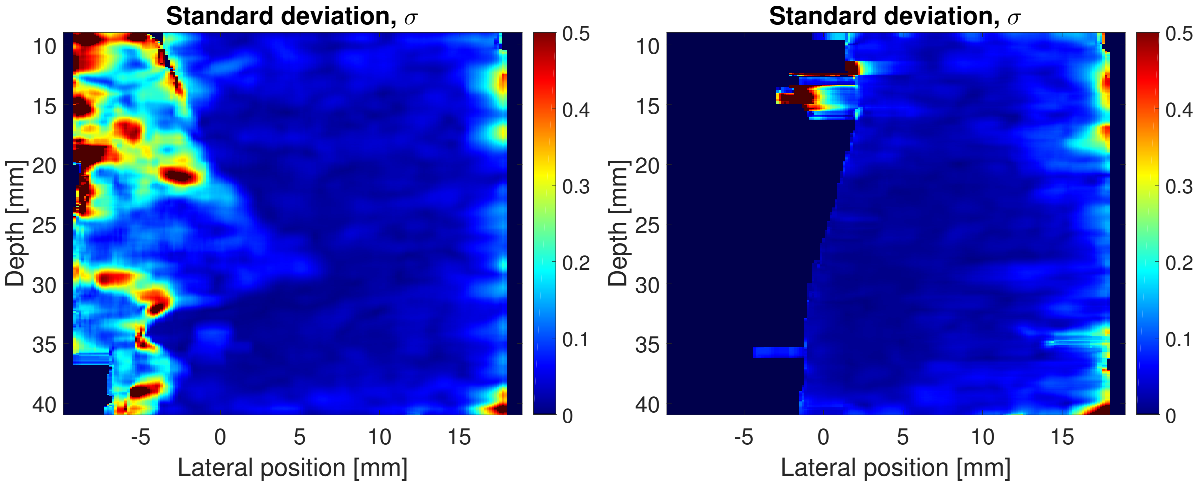

(c) 5 pushes, cross-correlation

(d) 5 pushes, cross-correlation + line detection

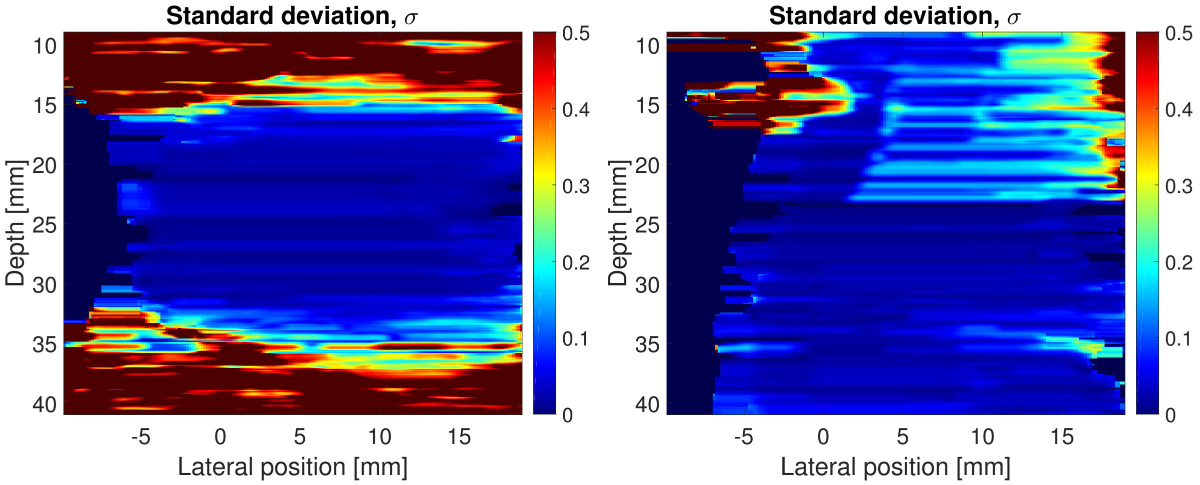

(e) 1 push, line detection

(f) 5 pushes, line detection

Figure 4.6: Standard deviation of the velocity estimates based on 10 samples each in a homogeneous medium. The single push is focused at 25 mm depth, the 5 push sequence is centered at 25 mm depth with 3 mm intervals between pushes.

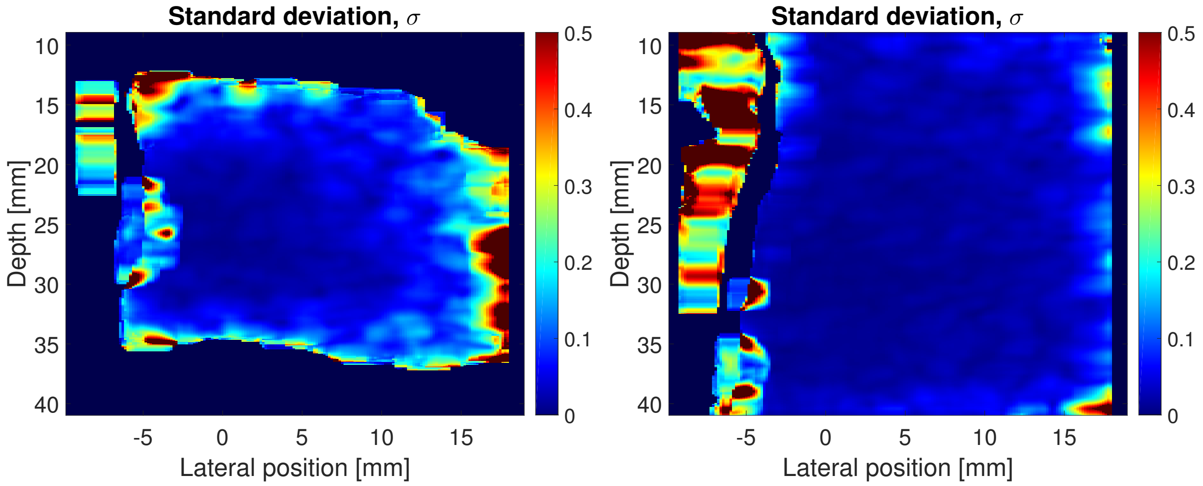

(g) 1 push, full-width cross-correlation.

(h) 5 pushes, full-width cross-correlation.

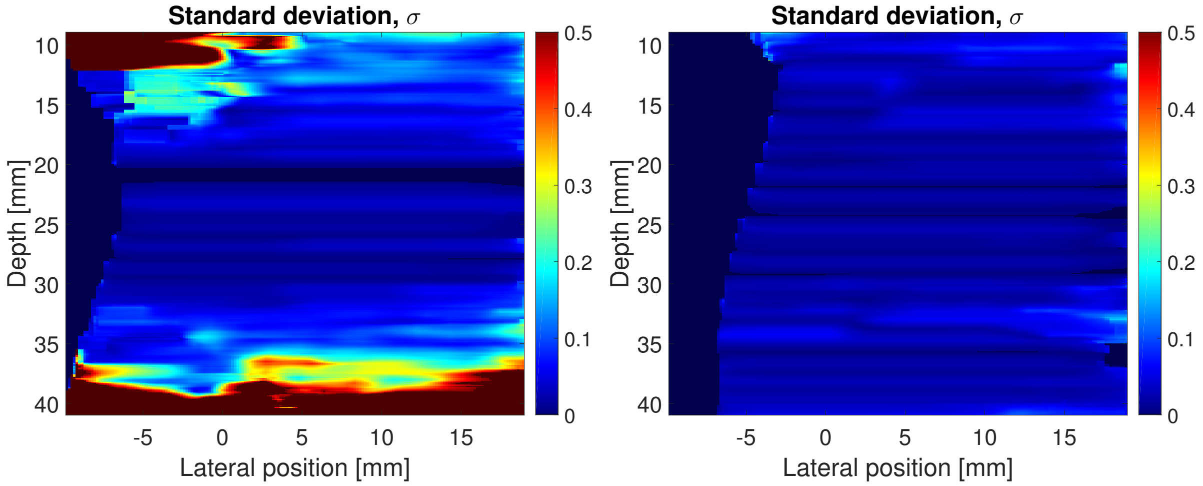

(i) 1 push, line detection with maximum amplitude.

(j) 5 pushes, line detection with maximum amplitude.

Figure 4.6: Standard deviation of the velocity estimates based on 10 samples each in a homogeneous medium. The single push is focused at 25 mm depth, the 5 push sequence is centered at 25 mm depth with 3 mm intervals between pushes. (cont.)

4.2.1 Bias and spatial variance

Figure 4.8 shows the velocity distribution of a representative part of the velocity estimates marked in Figure 4.7, in the homogenous phantom with an SSI sequence as shown in Figure 4.3. The edges of the boxes represent the 25th and 75th percentile of the data. The manually estimated velocity is based on 40 estimates performed by drawing lines along the tissue velocity maps in the same manner as the line detection, Figure 2.5 shows this method. Table 4.1 shows the sample standard deviation corresponding to the values used in Figure 4.8. It's worth noting that the average standard deviation (per pixel) when considering the same region across multiple measurements, as shown in Figure 4.6, is 0.0156 m/s for the full-width cross-correlation. Which is lower than all of the standard deviations estimated over the region.

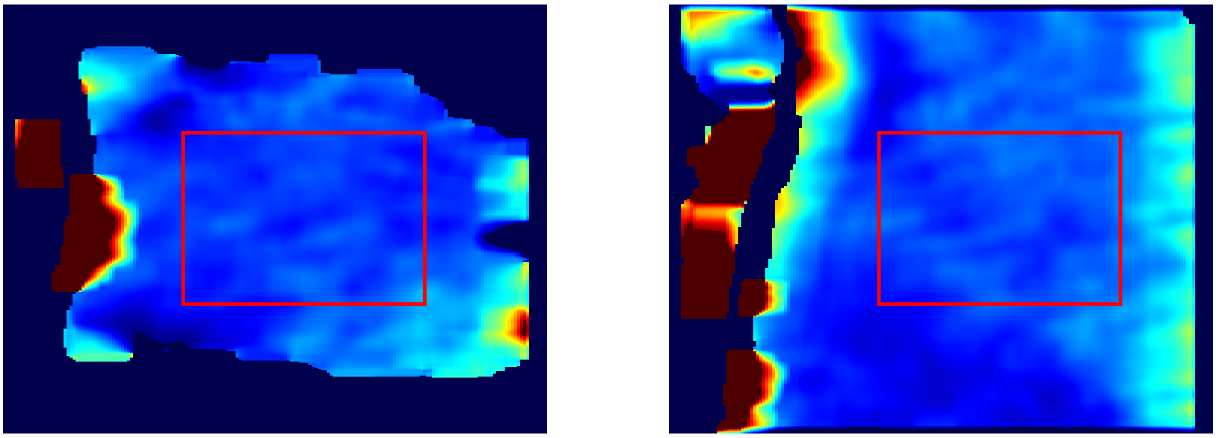

(a) 1 push

(b) 5 pushes

Figure 4.7: The red rectangle shows the selected data used to calculate the velocity distribution in Figure 4.8.

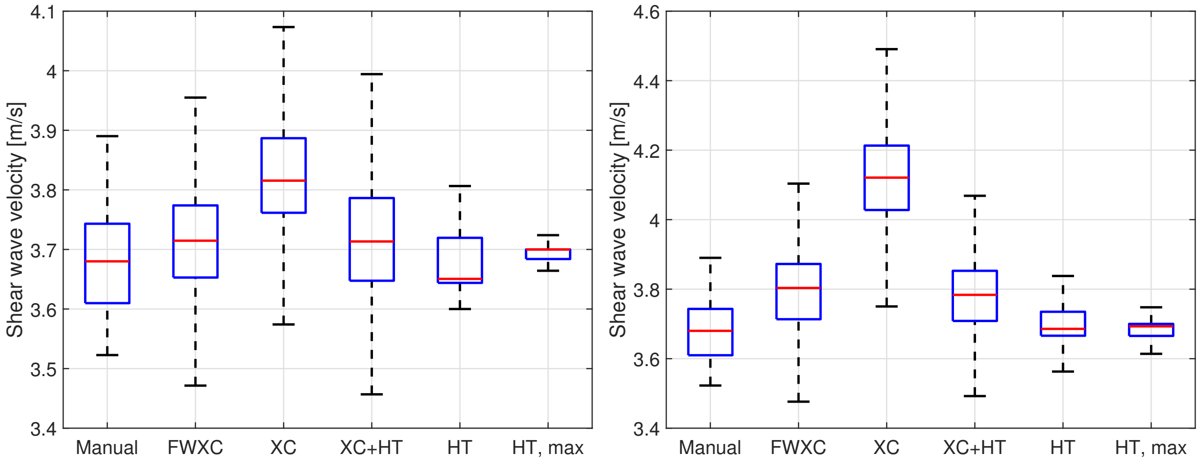

(a) 1 push (b) 5 pushes

Figure 4.8: Velocity estimation distribution for the regions shown in Figure 4.7. *Manual* is an estimate based on the velocity of 40 lines placed manually on the tissue velocity maps in the same manner as the line detection method. *XC* refers to cross-correlation, *HT* is the line detection using Hough transform, and *FWXC* is the full-width cross-correlation.

Table 4.1: Standard deviation estimated over the areas in Figure 4.7. Normalized by $N-1$ for N samples. *XC* refers to cross-correlation, *HT* is the line detection using Hough transform, and *FWXC* is the full-width cross-correlation. *HT, max* is the line detection method based on maximum amplitude of the tissue velocity map rather than edge detection.

SSI sequence	Estimation method	Standard deviation
1 ARF pulse	Manual	0.0978 m/s
	FWXC	0.1018 m/s
	XC	0.1101 m/s
	XC+HT	0.1256 m/s
	HT	0.0487 m/s
	HT, max	0.0160 m/s
5 ARF pulses	FWXC	0.1072 m/s
	XC	0.1476 m/s
	XC+HT	0.1176 m/s
	HT	0.1103 m/s
	HT, max	0.0348 m/s

4.2.2 Heterogeneous medium

The heterogeneous phantom was imaged as shown in Figure 4.9 with 5 ARF pulses focused outside of the soft cyst. The corresponding wave propagation is shown in Figure 4.10 where it's clear that the initial wavefront is plane, but it is quickly distorted by the cyst and other artifacts in the phantom. The estimated shear wave velocities in Figure 4.11 show significant differences between the different methods. All of the different methods manage to identify the soft cyst, but the line detection method has a poor estimate of the shape and size of the cyst, additionally the velocity of the surrounding medium is clearly overestimated. However, the line detection method is improved by using the maximum amplitude of the tissue velocities instead of edge detection. Using maximum amplitude, the velocity map offers better estimates in all regions, more accurate cyst shape and a very distinct boundary between the two mediums. The basic cross-correlation method shows the cyst, but has quite poor contrast and seems to have a lot of noise. Adding the line detection method to the cross-correlation data improves the contrast of the cyst, and the area lacking estimates with this method seems to be mostly poor estimates in the basic cross-correlation method. While none of the estimates improve significantly through temporal averaging of multiple measurements, the cross-correlation with line detection method appears to be the method that benefits the most. The best result was obtained through the full-width cross-correlation method, it has reasonable estimates both inside and outside the cyst, the the circular shape of the cyst is clear and the boundary between the mediums is more distinct than for either of the other cross-correlation methods. The sample standard deviation as shown in Figure 4.13 is clearly less smooth than for the homogeneous phantom, but it still provides mostly low variance for the full-width cross-correlation method.

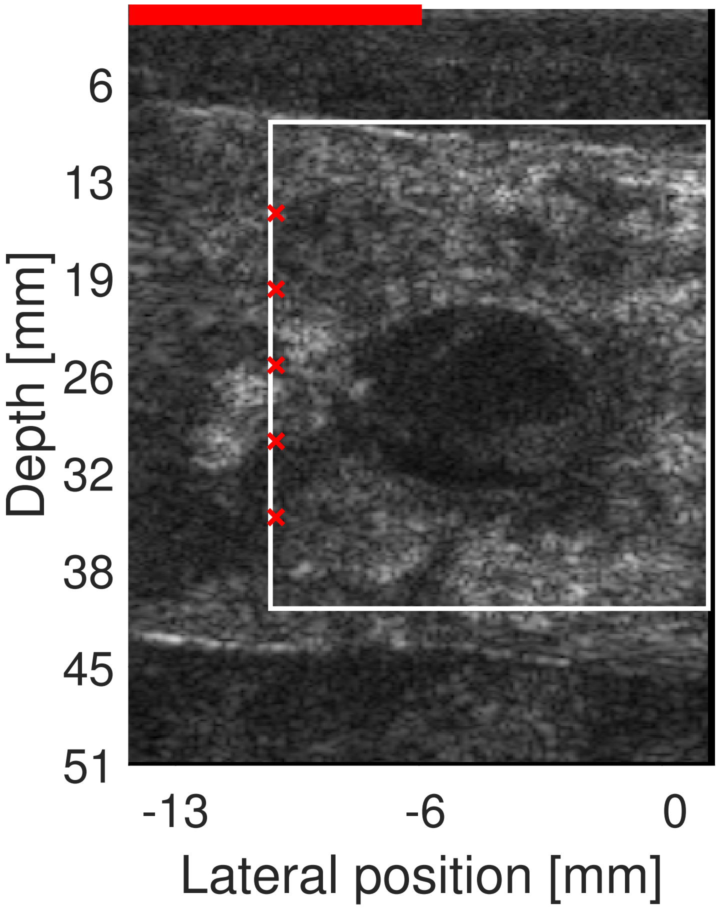

Figure 4.9: B-mode image of the heterogeneous phantom. The red crosses indicate the positions of the ARFI pulses in the 5 push sequences used for Figure 4.11 and Figure 4.10.

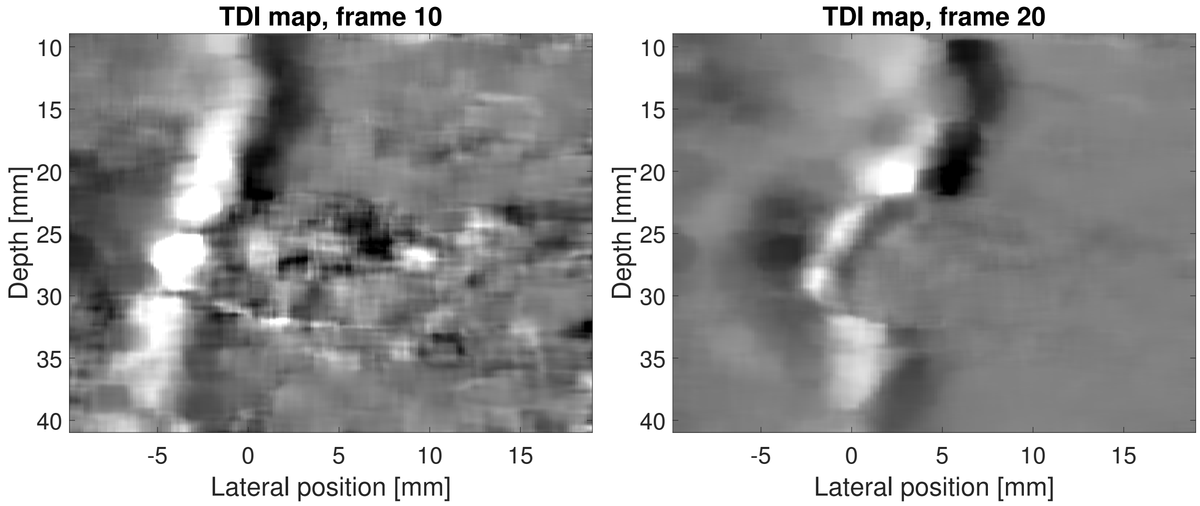

(a) Frame no. 10

(b) Frame no. 20

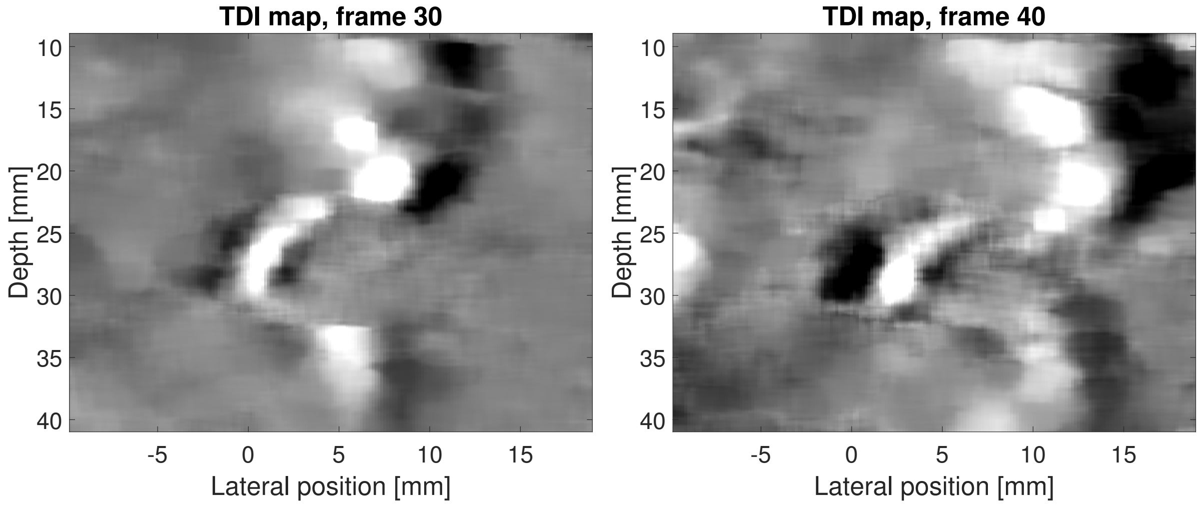

(c) Frame no. 30

(d) Frame no. 40

Figure 4.10: Tissue velocity from the TDI method for heterogeneous phantom. Corresponding to the shear velocity maps in Figure 4.11, and B-mode image in Figure 4.9.

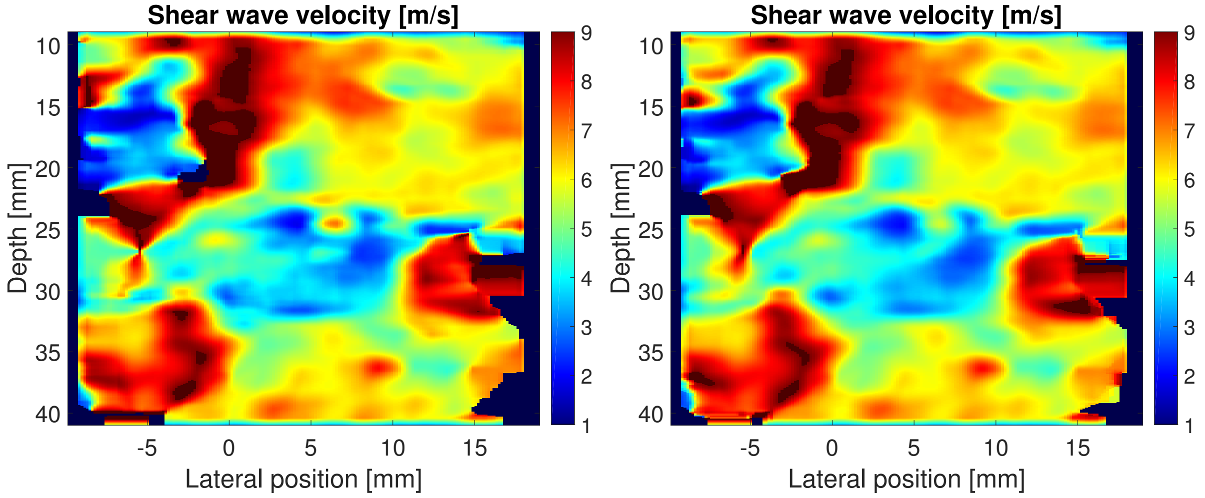

(a) Cross-correlation (b) Cross-correlation, avg. of 10 frames.

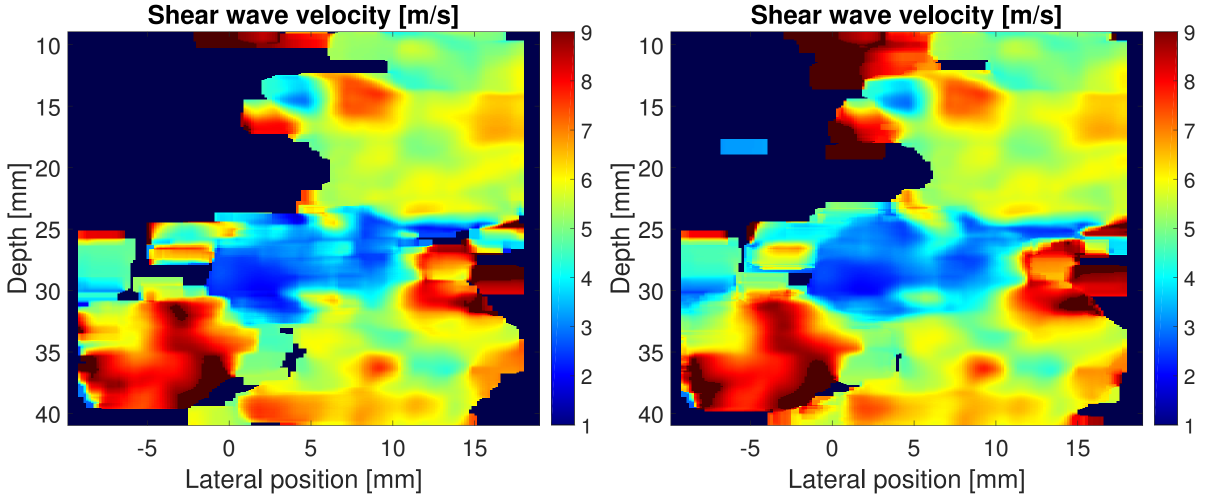

(c) Cross-correlation with line detection (d) Cross-correlation with line detection, avg. of 10 frames.

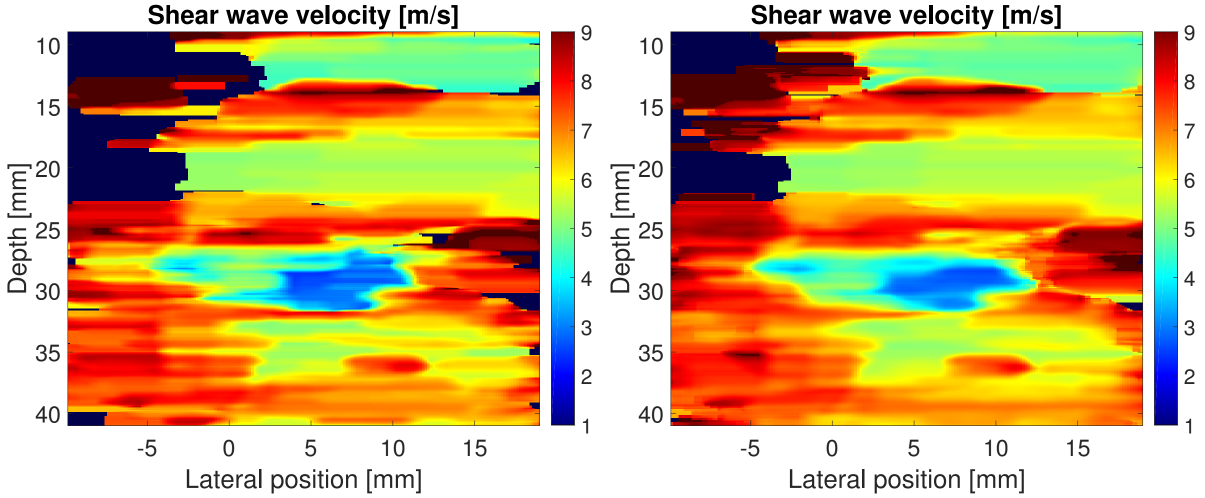

(e) Line detection (f) Line detection, avg. of 10 frames.

Figure 4.11: Shear wave velocity maps for a heterogeneous medium. 5 ARFI pushes with 5 mm intervals centered at 25 mm depth as shown in Figure 4.9.

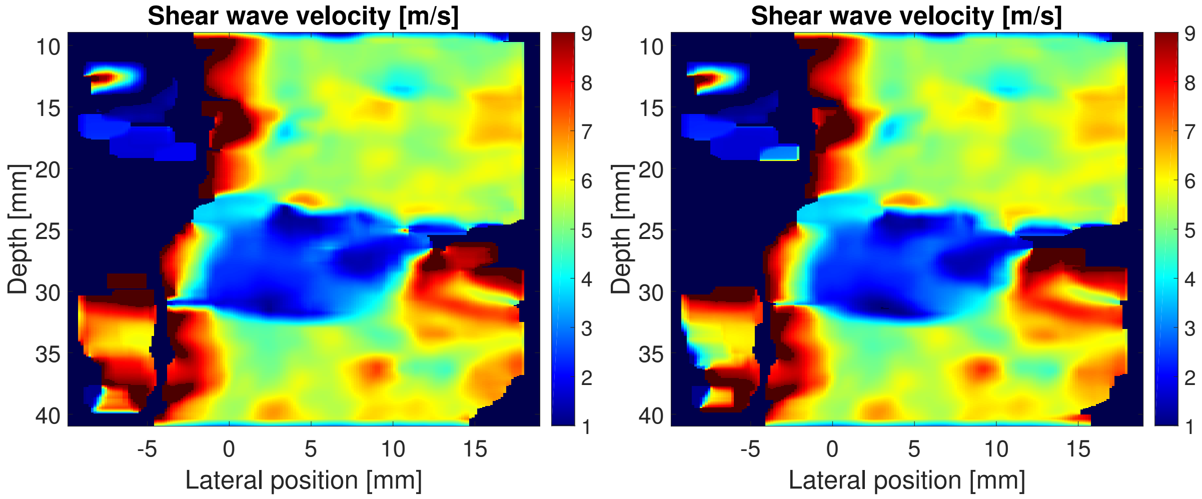

(a) Full-width cross-correlation

(b) Full-width cross-correlation, avg. of 10 frames.

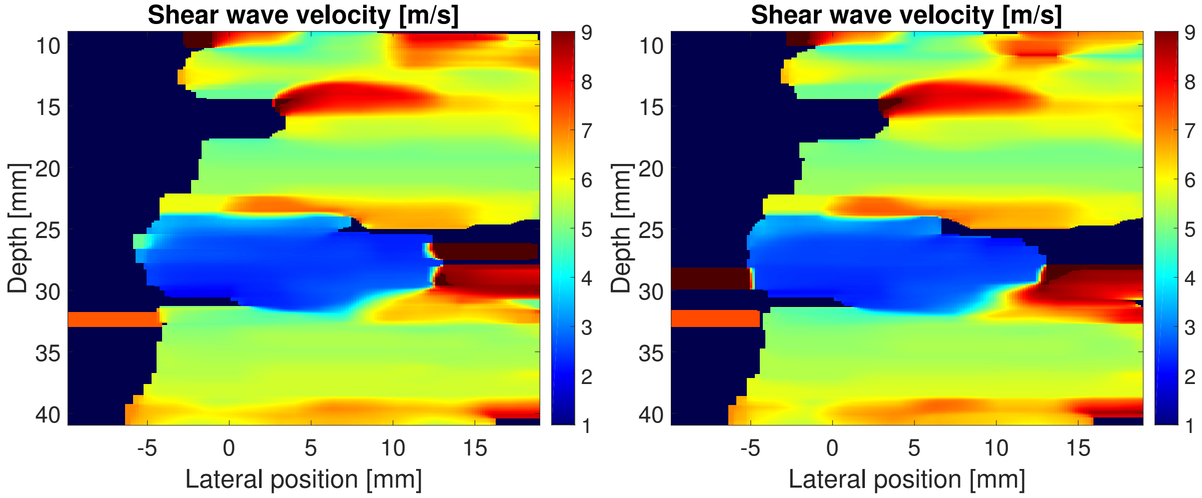

(c) Line detection with maximum amplitude

(d) Line detection with maximum amplitude, avg. of 10 frames.

Figure 4.12: Shear wave velocity maps for a heterogeneous medium. 5 ARFI pushes with 5 mm intervals centered at 25 mm depth as shown in Figure 4.9. (cont.)

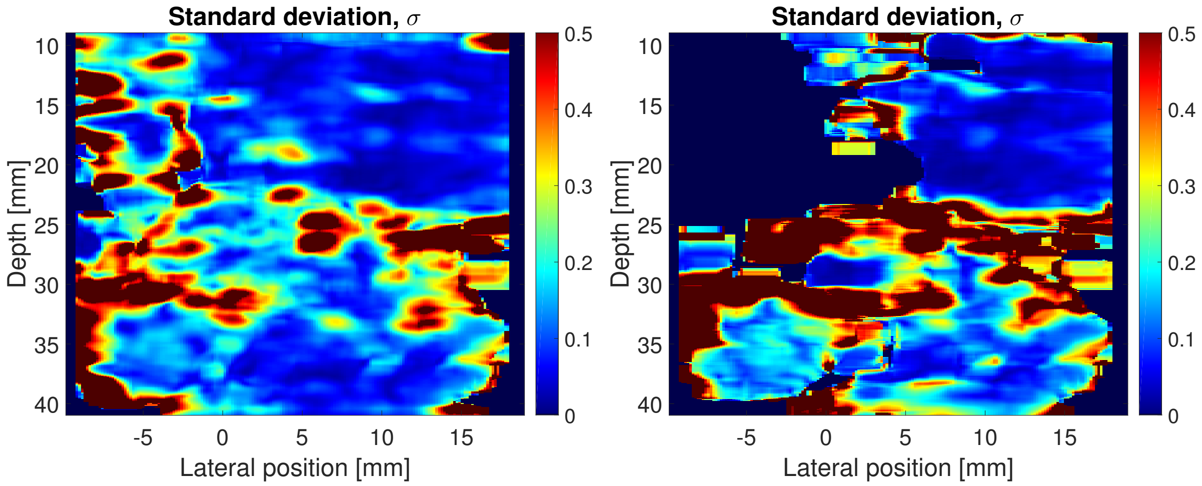

(a) Cross-correlation

(b) Cross-correlation with line detection

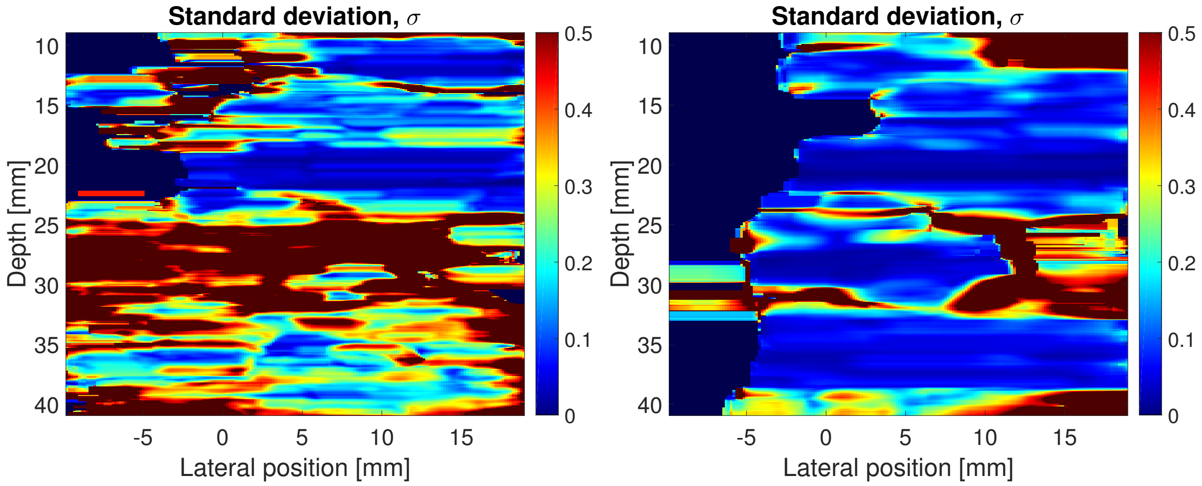

(c) Line detection

(d) Line detection with maximum amplitude

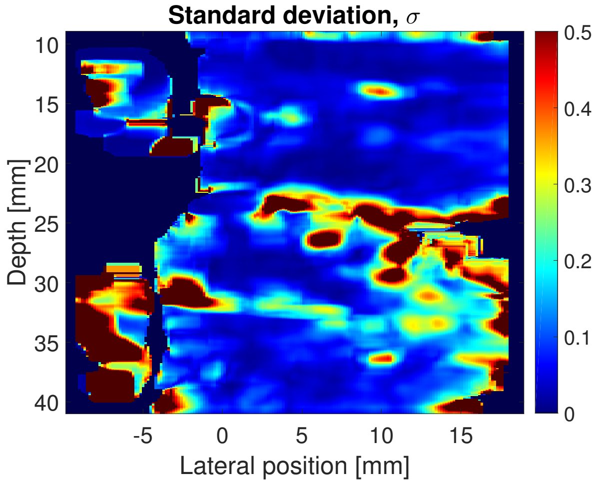

(e) Full-width cross-correlation

Figure 4.13: Standard deviation for the shear wave velocity estimates in Figure 4.11 based on 10 samples each. 5 ARFI pushes with 5 mm intervals centered at 25 mm depth in a heterogeneous medium as shown in Figure 4.9.

Internal reflections

Internal reflections can easily pose problems for the velocity estimates in heterogeneous mediums, and is likely a factor in the poor estimates for the heterogeneous phantom. This phenomenon can easily be demonstrated on a homogeneous phantom by placing the transducer parallel and close to one of the vertical phantom walls. Figure 4.14 shows the direct shear wave as a straight line, while the reflected wave shows up after about 4 ms. Because the reflected wave is coming in at different angles, the velocity appears higher than it is and might cause inaccurate estimates.

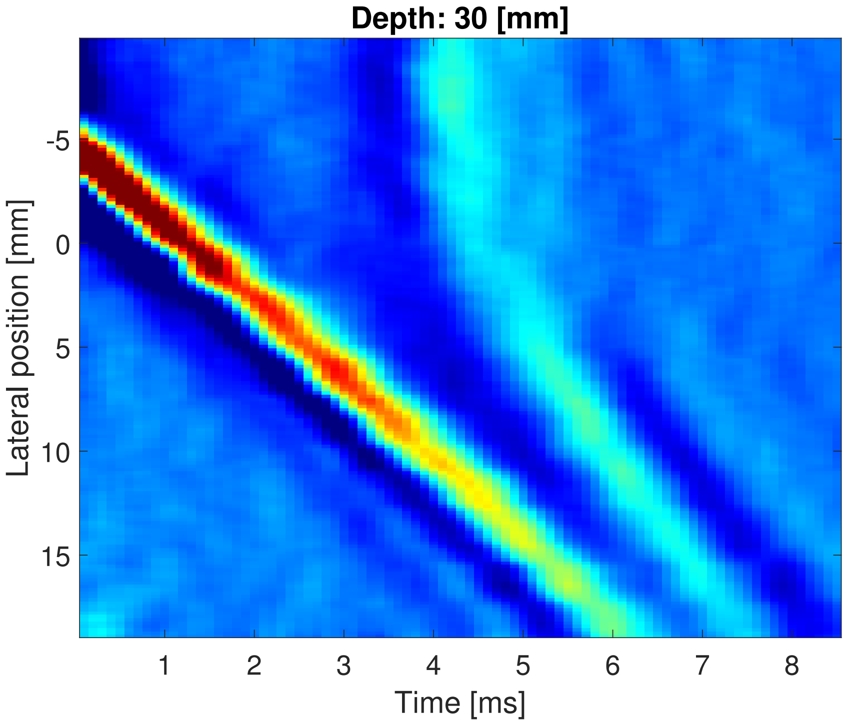

Figure 4.14: Tissue velocity map in a homogeneous medium with wall reflections coming in after ~4 ms.

These reflections can also be seen in the heterogeneous phantom. In Figure 4.15, parts of the SSI sequence are focused inside the cyst. The shear wave inside the cyst is clearly seen in the tissue velocity map in Figure 4.16a. The shear wave is propagating slowly through the cyst until it reaches the harder surrounding medium at about 2 mm lateral position, where the shear wave continues at a higher velocity. Because of the reflection at the interface between the two mediums, the shear wave transferred into the harder medium is noticably weaker.

The velocity maps in the following sections will use full-width cross-correlation unless otherwise specified.

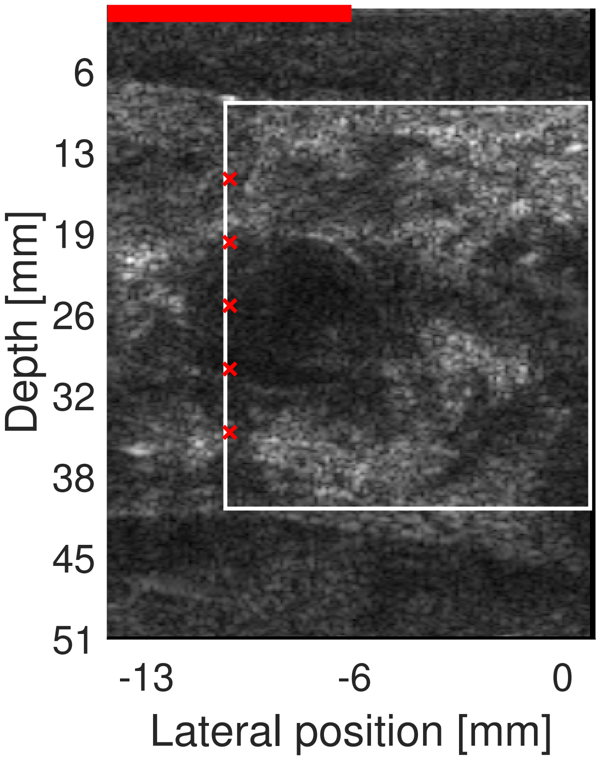

Figure 4.15: B-mode image of SSI sequence partially inside cyst.

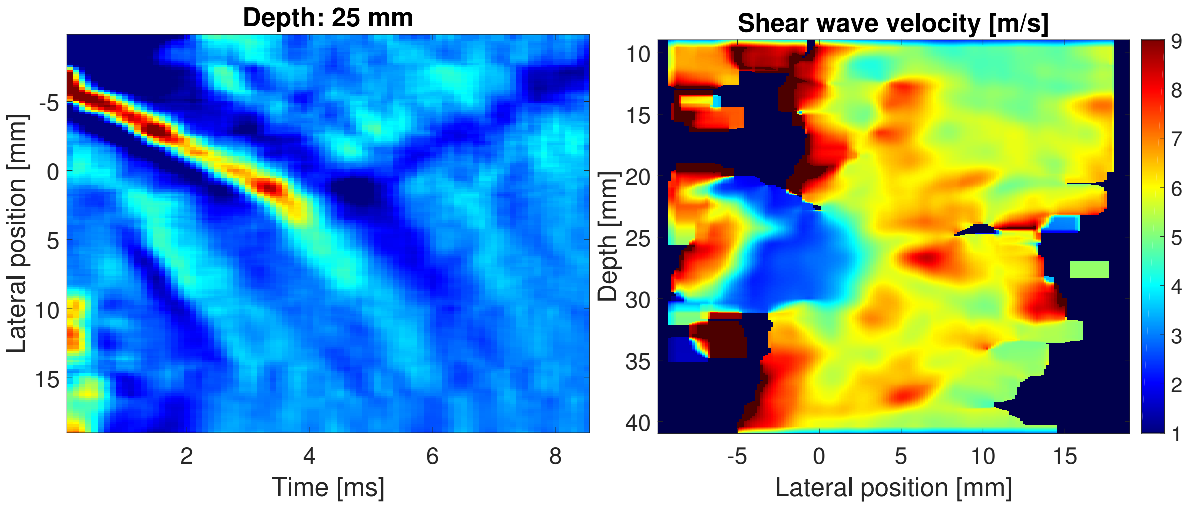

(a) Tissue velocity map showing a shear wave propagating through a soft cyst and into a harder medium with reflections.

(b) Shear wave velocity map, full width cross-correlation

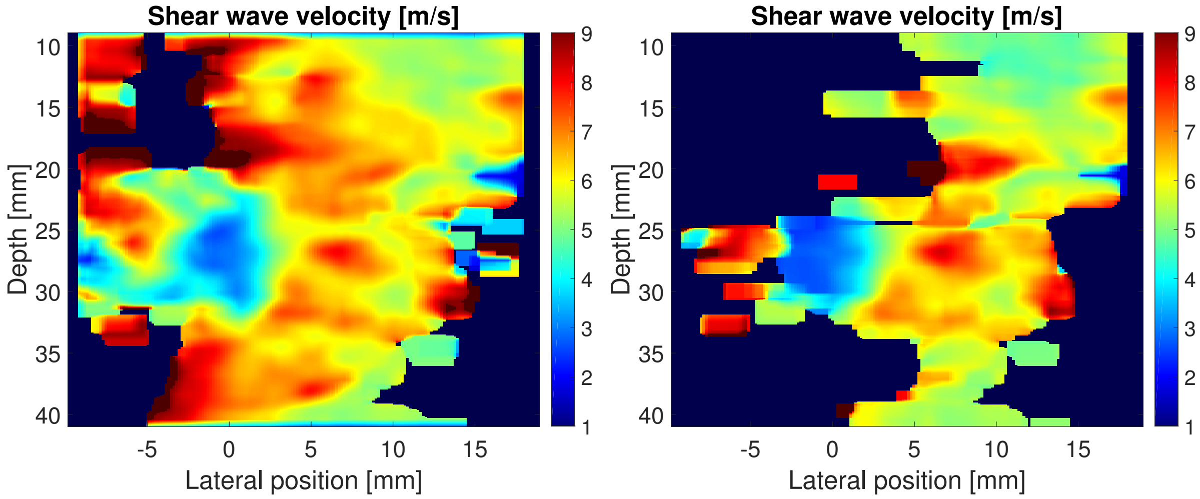

(c) Shear wave velocity map, cross-correlation

(d) Shear wave velocity map, cross-correlation and line detection

Figure 4.16: Tissue velocity and shear wave velocity for the SSI sequence shown in Figure 4.15. While the combination of cross-correlation and line detection shows the cyst clearly, it also has no estimates for a large area surrounding it

4.3 Push sequences at different depths

All the results presented so far have been based on an ARF pulse focused at 25 mm depth, or an SSI sequence with a range centered at 25 mm. The velocity maps in Figure 4.17 present the estimated velocity based on a single ARF pulse focused at different depths from 5 mm to 45 mm. At very close range, there are quite large angles from the transducer elements at the edge to the focal point, which means the beam pattern of the transducer elements will affect the excited radiation force. As a result, the estimates from a 5 mm focus are very poor, and the shear wave velocity map for a 10 mm appears to offer better estimates, even at 5 mm. As the focal depth increases, the range of reasonable estimates also increase, at 40 and 45 mm focal depth, there are reasonable velocity estimates in the entire ROI range. This is caused by the fact that the "region" of the focal point is larger in the axial direction than lateral, which means the shear wave "source" spans a longer distance in axial direction. Additionally, the aperture is the same for all distances, which means that the signal at focal depth will be less focused at greater depths.

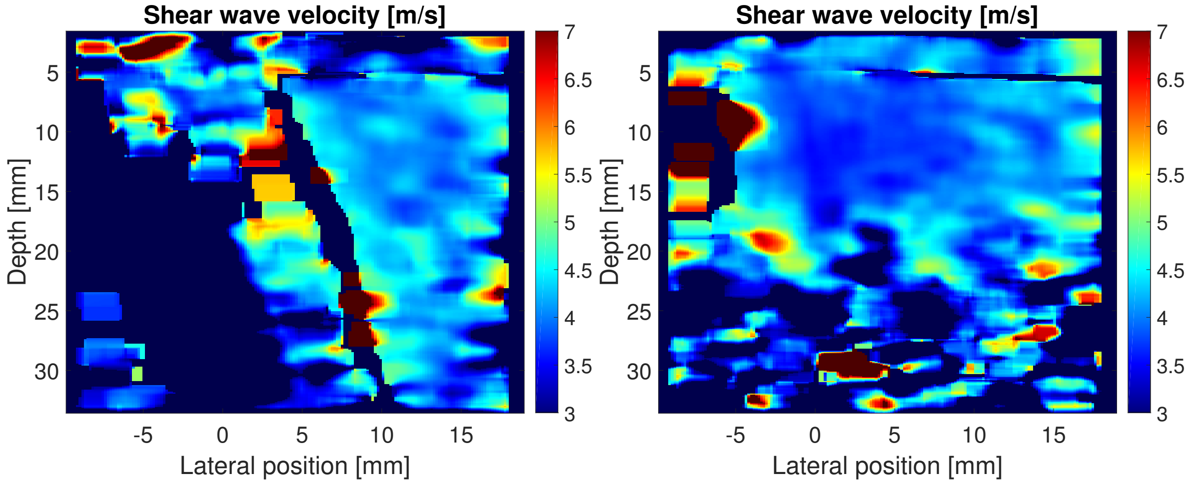

(a) 5 mm (b) 10 mm

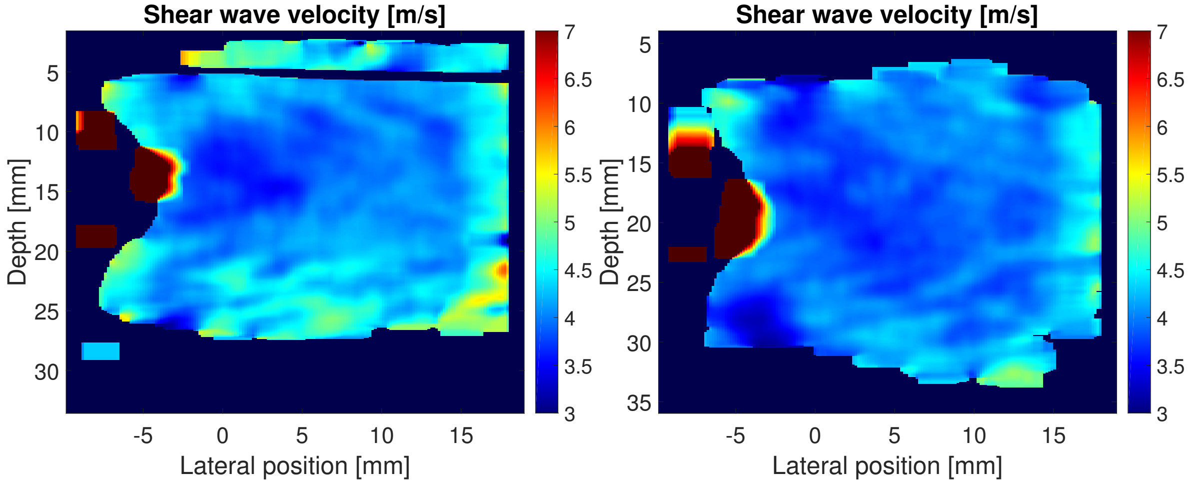

(c) 15 mm (d) 20 mm

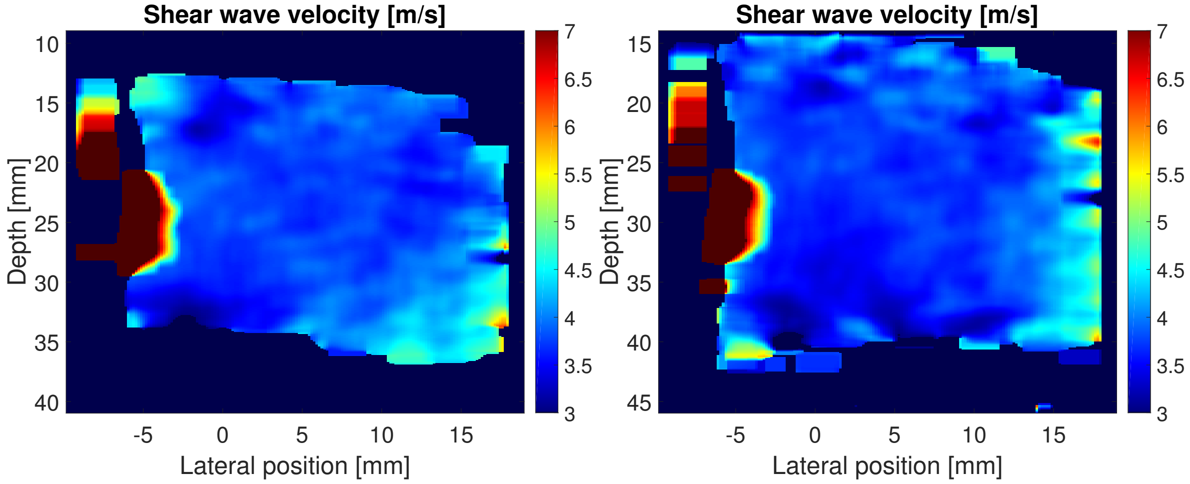

(e) 25 mm (f) 30 mm

Figure 4.17: Shear wave velocity maps based on a single ARF pulse, focused at different depths.

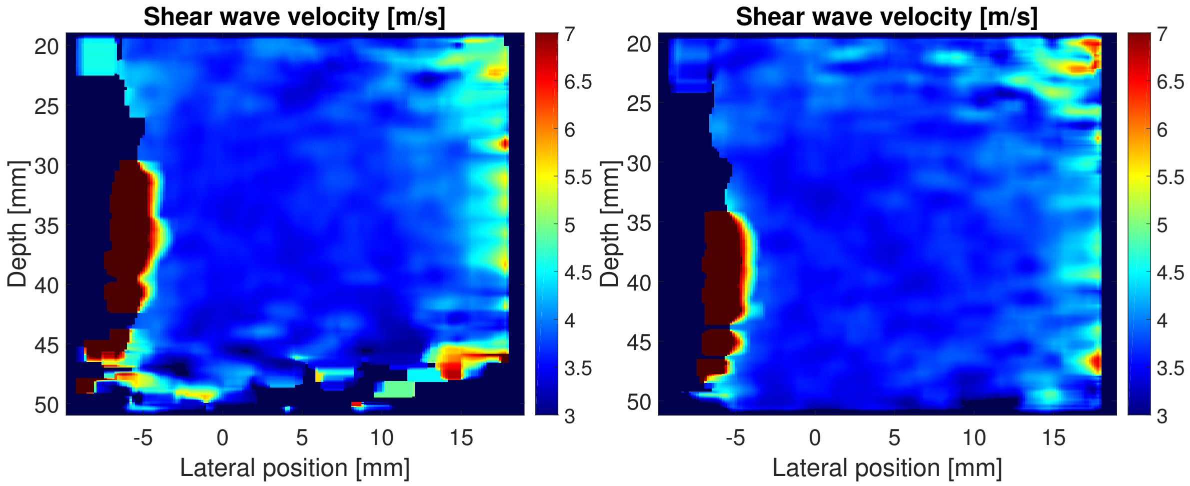

(g) 35 mm (h) 40 mm

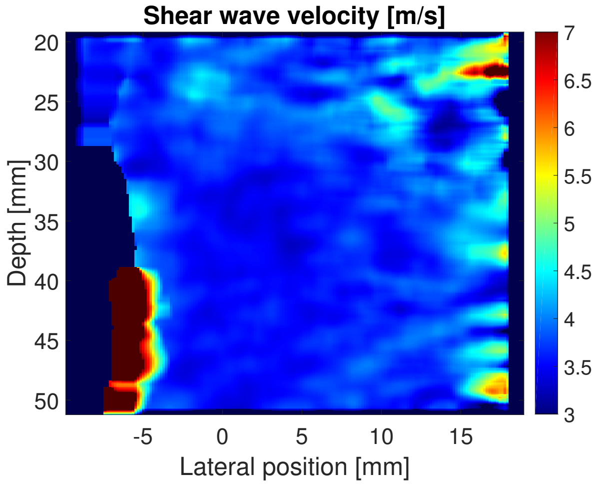

(i) 45 mm

Figure 4.17: Shear wave velocity maps based on a single ARF pulse, focused at different depths. (cont.)

4.4 Multi-purpose phantom

The multi-purpose phantom from CIRS was imaged as shown in Figure 4.18. The phantom contains three cysts with different elasticity, they have Young's modulus of 10, 40 and 60kPa. The elasticity of the surrounding tissue was not known. In order to compare to the known elasticity parameters, the shear wave velocities were converted to Young's modulus with the assumption that the phantom had a mass density of $1000\,\mathrm{kg/m^3}$ and a Poisson's ratio of 0.5, giving the direct relation of $E = 3000c_t^2$ as given by equation (2.6). Figure 4.18 shows the B-mode images of the different cysts, and it's clear that the contrast is very low as it's hard to see the cysts even with knowledge about where they should be. However, the elasticity images in Figure 4.19 show the cysts more clearly, the hard cyst in particular is clearly stiffer and has a reasonably well defined shape. The soft cyst is also clearly softer than the surrounding tissue, even though the boundaries of the cyst are not as well defined considering the difference in Young's modulus is less. The 40 kPa cyst is the hardest one to spot, and it's not clear from the elasticity map that there is a circular cyst there, although there is a slightly stiffer area in the middle. Table 4.2 shows the estimated Young's modulus averaged over representative regions for each cyst and the surrounding medium. None of the cysts are accurately estimated, and the bias is not consistent between cysts. It may seem like the estimates are compressed relative to the expected Young's modulus.

Table 4.2: Estimated Young's modulus for multi-purpose phantom

Tissue, expected E	Estimated E
Surrounding, unknown	$24.7 \pm 2.2\,\mathrm{kPa}$
Cyst, 10 kPa	$16.0 \pm 1.1\,\mathrm{kPa}$
Cyst, 40 kPa	$30.6 \pm 2.7\,\mathrm{kPa}$
Cyst, 60 kPa	$37.9 \pm 3.5\,\mathrm{kPa}$

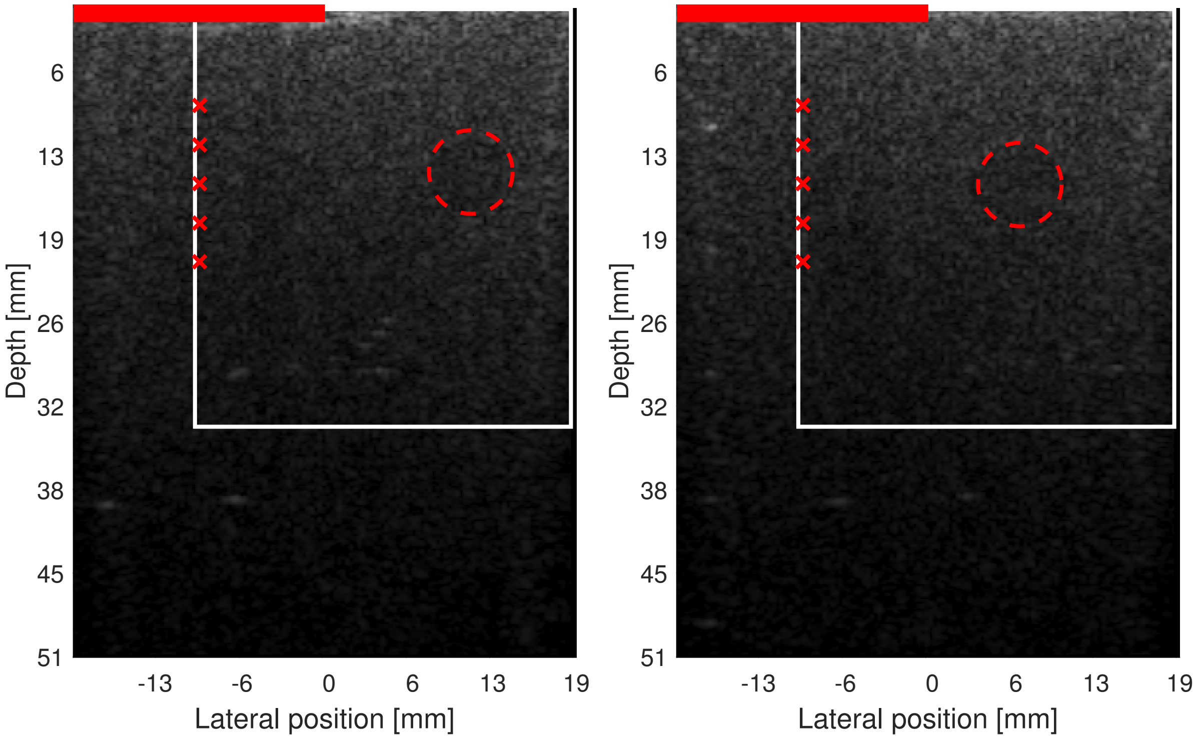

(a) Hard cyst, 60 kPa (b) Medium cyst, 40 kPa

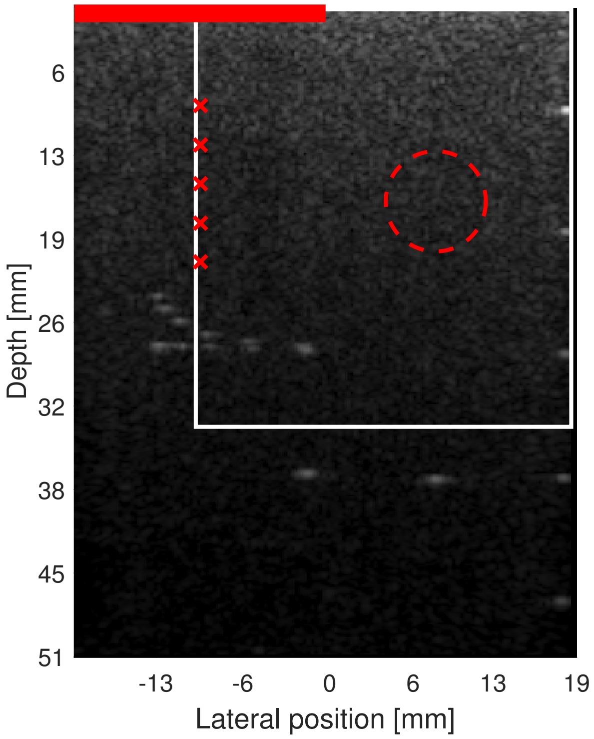

(c) Soft cyst, 10 kPa

Figure 4.18: B-mode image of the three different cysts in the multi-purpose phantom, the cysts are marked with a red circle as they are very difficult to see on the B-mode image.

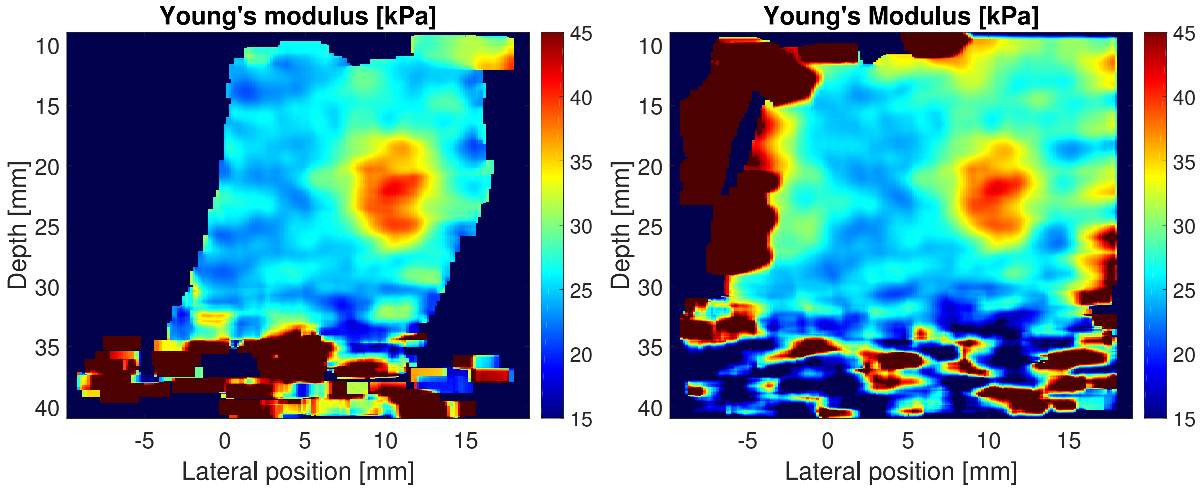

(a) Hard cyst, 60 kPa, cross-correlation with line detection

(b) Hard cyst, 60 kPa, full-width cross-correlation.

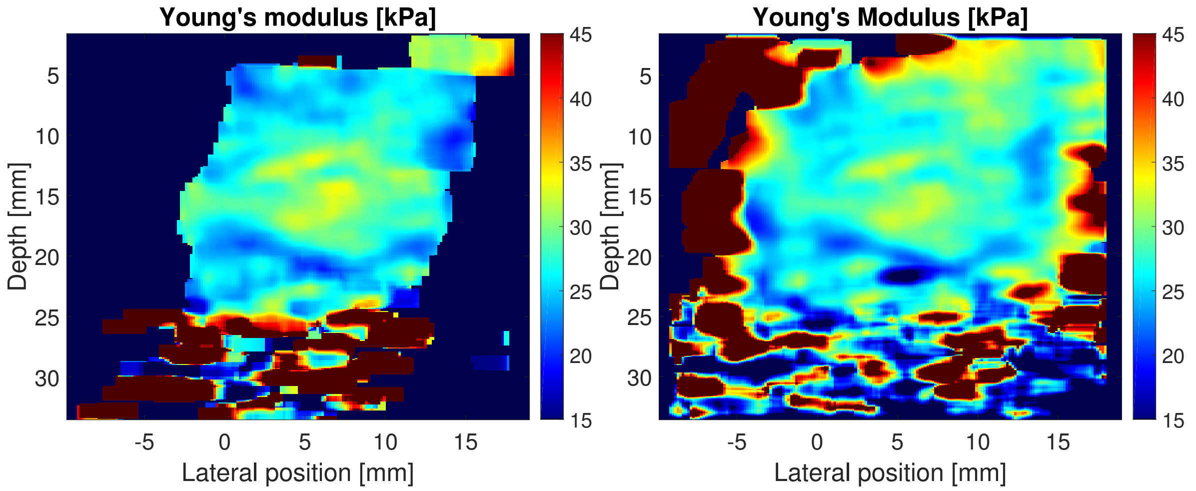

(c) Medium cyst, 40 kPa, cross-correlation with line detection

(d) Medium cyst, 40 kPa, full-width cross-correlation.

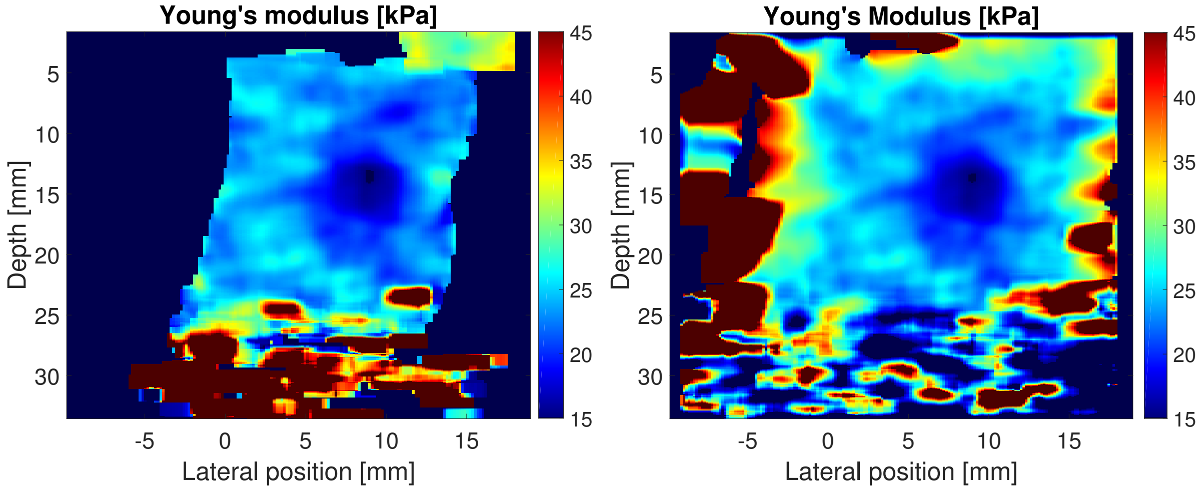

(e) Soft cyst, 10 kPa, cross-correlation with line detection

(f) Soft cyst, 10 kPa, full-width cross-correlation.

Figure 4.19: Young's modulus of the three different cysts in the multi-purpose phantom. Both the hard cyst and the soft cyst are easily identified, although the elasticity estimate is biased. Both the full width cross-correlation and the combined cross-correlation and line detection methods are shown.

4.5 Dual transducers

Because the two probes could not be placed perfectly parallel on a line on the same phantom, the shear wave velocities estimated with two transducers were slightly higher.

With the dual transducer setup, the shear waves need to travel for some distance before they reach the ROI of the imaging transducer. This means that we can easily image the shear wave across the entire lateral range of the ROI as shown in Figure 4.20. It's clear from both the tissue velocity maps and the shear wave velocity maps (Figure 4.21) that there is more noise when only a single ARF pulse is used to excite shear waves.

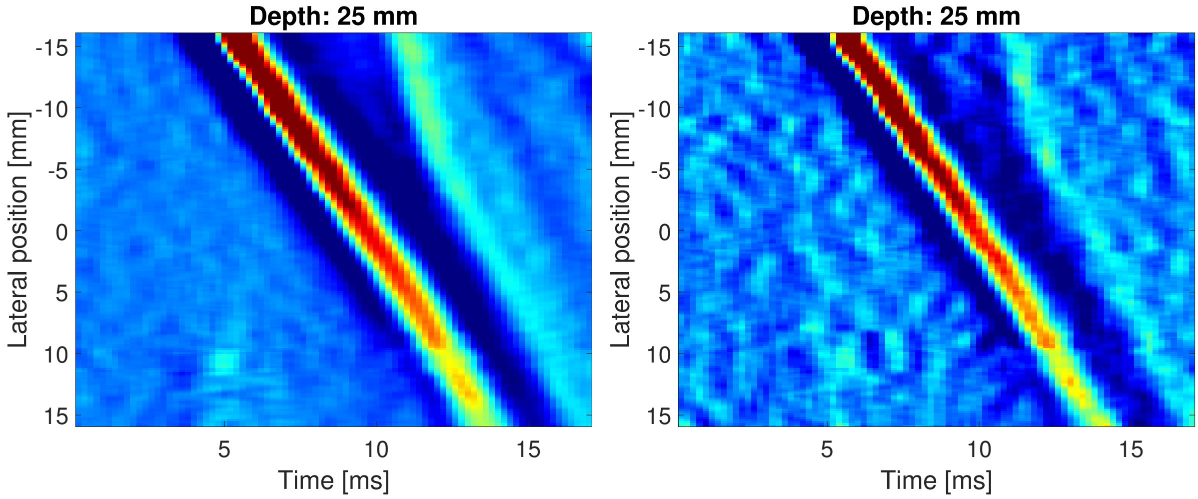

(a) 5 pushes, 5 mm intervals

(b) 1 push

Figure 4.20: Tissue velocity (TDI) map from a dual transducer setup with a homogeneous phantom, ARF pulses focused at 25 mm depth.

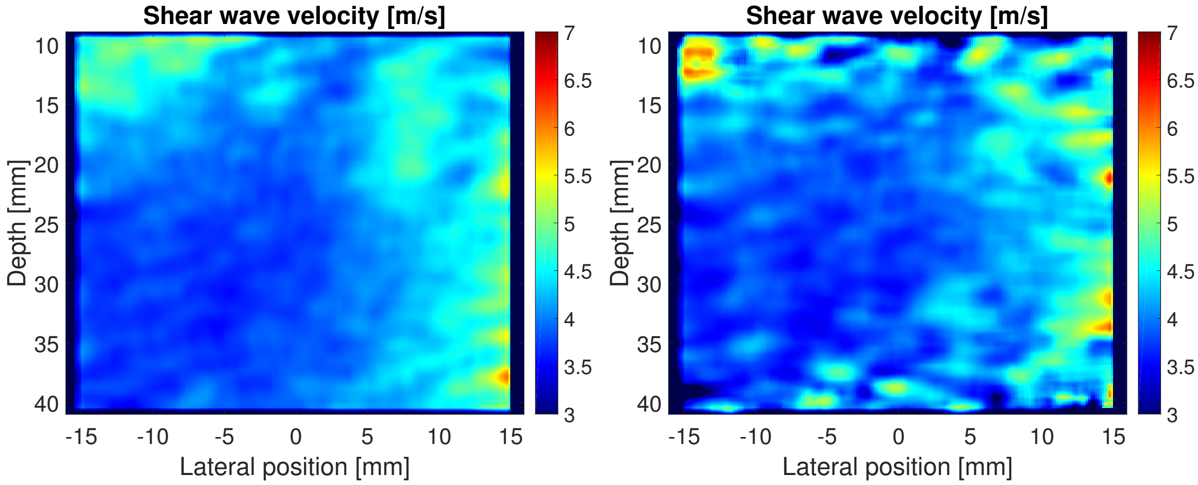

(a) 5 pushes, 5 mm intervals

(b) 1 push

Figure 4.21: Shear wave velocity maps from a dual transducer setup with a homogeneous phantom, ARF pulses focused at 25 mm depth.

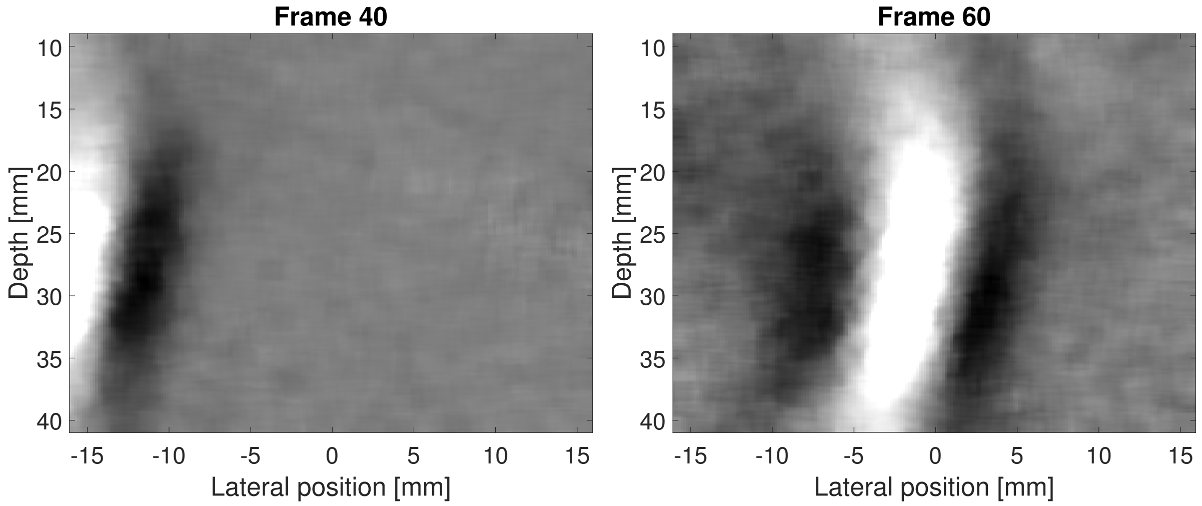

(a) Frame no. 40

(b) Frame no. 60

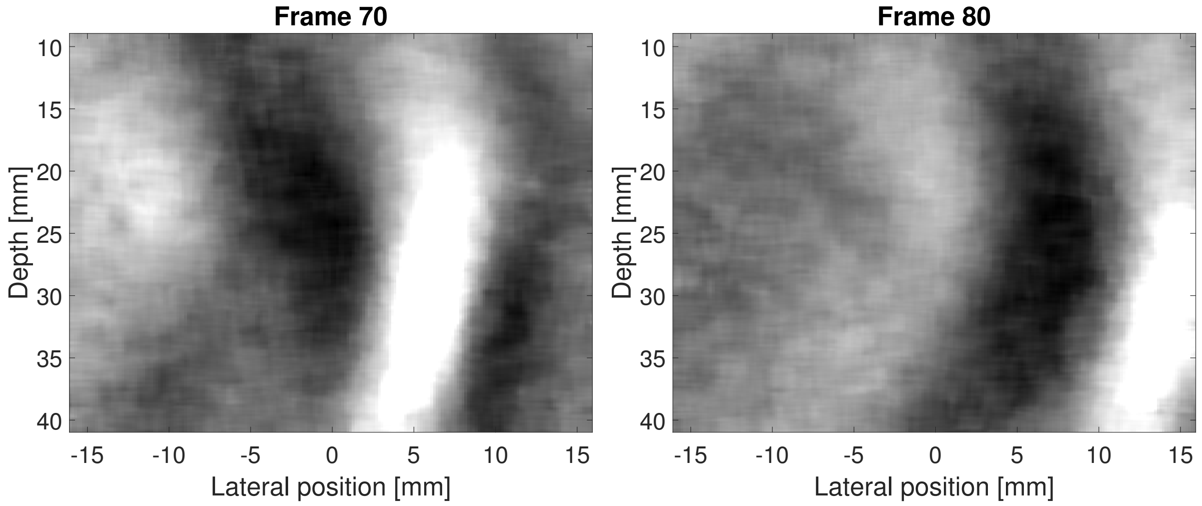

(c) Frame no. 70

(d) Frame no. 80

Figure 4.22: Tissue velocity from the TDI method for homogeneous phantom with dual transducer. Corresponding to the shear velocity maps in Figure 4.21.

4.6 Thermal measurements

Even with low frame rates, the high voltage and PRF used caused significant temperature rise very quickly.. A "frame" in this context refers to the shear wave velocity maps, each generated by an SSI and imaging sequence. Figure 4.23 shows the temperature for two measurements in air with a peak-to-peak amplitude of 70 V for both pushing and imaging, 5 ARF pulses, 10 ms of imaging per sequence, and a frame rate of 3.3 frames per second (FPS), and central frequency of 4.8 MHz. The figure shows a temperature increase of 10 °C as a dashed line, for the sequences with 5 kHz PRF it took 32 s to increase the temperature by 10 °C, and with an imaging PRF of 10 kHz this time was reduced to 10 s as shown in Table 4.3. The temperature rise was also measured on a phantom, with transmission gel to ensure proper conduction. The rise in temperature was significantly slower, but still increased by more than 10 °C in less than 4 minutes as shown in Figure 4.24 and Table 4.3.

Figure 4.24b shows a significant difference between ambient and transducer temperature, this was caused by the phantom still being cold after being taken out of the fridge, and the ambient temperature sensor was placed on the phantom in a location that might've been slightly better insulated. The measurement was deemed reasonable considering it's unlikely that more precision would impact the result in any meaningful way.

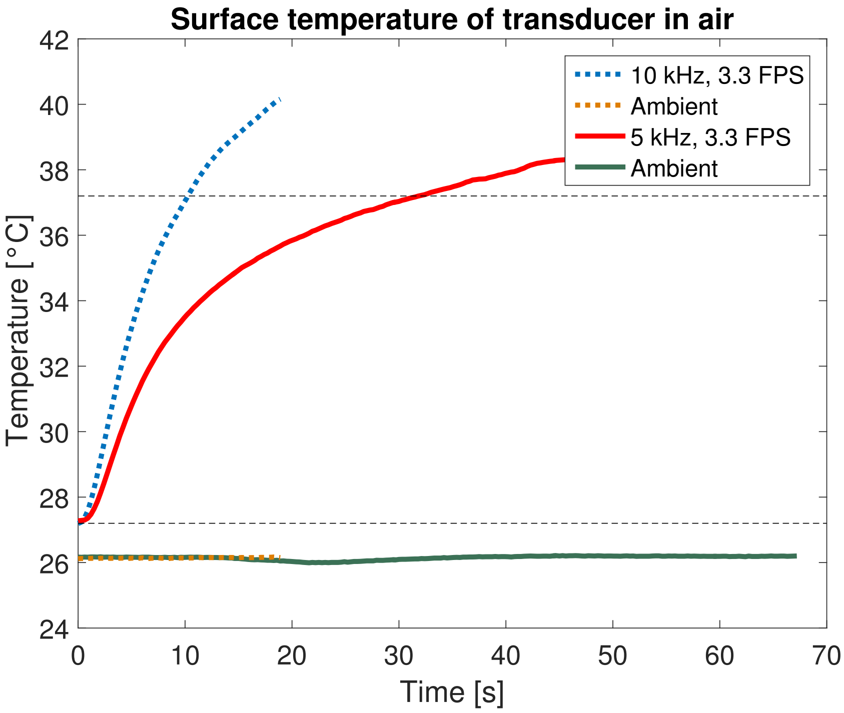

Figure 4.23: Surface temperature of a transducer in air for an SSI sequence with 5 ARF pulses, 10 ms of imaging with a PRF of 10 kHz, amplitude of 70 V peak-to-peak, and sequence rate of 3.3 FPS.

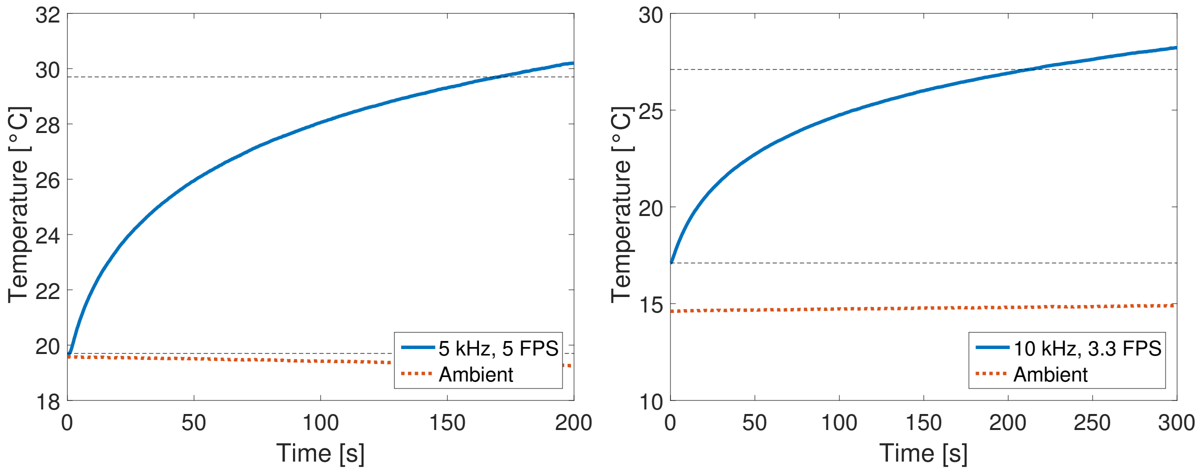

(a) 5 kHz PRF, 5 FPS (b) 10 kHz PRF, 3.3 FPS

Figure 4.24: Surface temperature of transducer on a PVA phantom.

Table 4.3: Time for surface temperature of transducer to increase by 10 °C for different mediums and sequence parameters.

Medium	PRF	FPS	$t_{\Delta 10\,^{\circ}\mathrm{C}}$
Air	5 kHz	3.3	32 s
Air	10 kHz	3.3	17 s
Air	5 kHz	5	10 s
Phantom	5 kHz	5	170 s
Phantom	10 kHz	3.3	212 s

Chapter 5

Discussion

This chapter discusses the results presented in the previous chapter, what they mean for practical implementations, what concerns are raised, and what directions would be natural to explore in the future.

Figure 4.1 clearly demonstrates the impact of SSI on the shear wave propagation, by increasing the number of pulses used, a larger area (in axial direction) is covered as shown in the difference between Figure 4.4b and d. The wavefront also becomes nearly plane, ensuring that the propagation in lateral direction is representative of the shear wave velocity at all depths. The constructive interference also increases the amplitude of the shear wave, which makes the elasticity estimates accurate over a longer distance in lateral direction. This is demonstrated by the more prominent background noise found in Figure 4.1c, showing normalized tissue velocity for a single ARF pulse. The increased noise level is perhaps most apparent in the dual transducer setup, Figure 4.20 shows the tissue velocity at the focal depth with both 5 and 1 ARF push, with significantly higher noise levels for the single push case. The reduced noise leads to a smoother shear wave velocity map in Figure 4.21 for the SSI sequence.

It's interesting to note, that the small local variations in velocity estimates are consistent across separate measurements. The estimated standard deviation between frames is consistently very low (typically $<0.1\,\mathrm{m/s}$ for homogeneous phantom) for measurements with the same settings, while the local variations in velocity for the same regions are higher, as can be seen by Table 4.1. The local variations might be caused by speckle noise, in which case employing one or more compounding techniques could be beneficial. Angle compounding of the plane imaging is a technique that has been employed to increase image quality and reduce speckle noise for SWE methods before [27], [28], and would be a natural consideration in future efforts to improve the technique presented. Shear compounding would be another option, combining the results of SSI sequences with different distances between ARF pulses to generate wavefronts with different angles [20]. However this requires multiple SSI sequences for each velocity estimate and would be sensitive to any movement of the probe or tissue.

The heterogeneous phantom used for these measurements clearly had more variance than intended, instead of two homogeneous mediums combined, there were irregularities throughout the entire phantom. It also had considerable bacterial growth, far more than the much older homogeneous phantom. It's entirely possible that the elastic properties of the phantom changed significantly throughout the project as a result of this, but all the measurements for the heterogeneous phantom presented in this report were performed on the same day. These irregularities could be a result of the production process not being done properly, in particular it was seen that the heated PVA mixture was not heated homogeneously as the mixture in the middle of the container did not melt properly and caused small particles in the liquid. It could also be an issue with freeze-thaw cycle, the phantom was manually put into, and out of a freezer which will cause an immediate change in ambient temperature. A more gradual change in temperature would give more even temperature throughout the phantom, which might have impact on the homogeneity. Finally, it's worth noting that the artifacts observed in this phantom also became an issue for other phantoms made around the same time, a plausible explanation would be that the PVA powder was spoiled by humidity.

The irregularities of the heterogeneous phantom makes it difficult to assess the estimated velocities as there is no clear expectation about what the estimated values should be. However, it does serve to highlight some of the difficulties involved with localized estimation of shear waves in complex mediums, both in terms of the implementation presented here, and for SWE in general. The cross-correlation method assumes similarity between the tissue velocity signals at different lateral positions and uses the correlation lag between two time signals to estimate the velocity. The difference between two adjacent signals can be very small and more sensitive to noise than the difference between signals further apart. The estimates in this report compares lines that are 4 mm apart and employs subpixel estimation of the correlation lag to reduce the impact of noise on the estimate. However this also means that the spatial resolution is reduced, the estimated velocity will be the average velocity between the two correlated lines. The cross-correlations are still iterated one pixel at a time, which means that smaller variations can be detected, but the velocity estimate will be biased towards the average in the range. For the phantoms and resolutions considered in this report, these values were considered to give a reasonable trade-off between spatial resolution and noise resiliency, but it’s important to keep in mind as it’s one of the parameters with the highest impact on the velocity estimates.

The difference between the correlation of shorter time segments and using the full range possible was also shown. For the heterogeneous PVA phantom the velocity estimation was smoother and with a more distinct cyst when using cross-correlation with the full length of the time data. Using shorter time segments combined with line detection to select the most relevant segments was the other approach that achieved good results, but for the heterogeneous PVA phantom there were more irregularities and a larger area without valid estimates. In contrast, the results from the multi-purpose phantom were very similar, but while the "full-width" approach had areas with clearly inaccurate estimates, the cross-correlation and line detection method instead considered those estimates to be invalid. Some of the discrepancy between the two methods can be reduced by adjusting the cross-correlation coefficient threshold used to detect valid estimates, but even then the full width approach seemed to be more prone to include inaccurate estimates.

A very basic velocity estimation technique is to select the maximum values for each lateral position and use linear regression, but this method is only reasonable for truly homogeneous mediums. The Hough transform-based line detection algorithm presented in this report is an attempt at expanding that concept to heterogeneous mediums. Unsurprisingly, the method worked well for homogeneous phantoms with reasonable velocity estimates. However, the lines necessarily need to have a minimum length which means the resolution was quite bad. A lower threshold for valid lines would potentially allow for better spatial resolution, but it would also increase the number of spurious lines detected. Lines caused by reflections and noise are already an issue with this approach and would potentially be worsened by allowing shorter line segments. Using the maximum values of the TDI-map instead of the LoG-based edge detection was shown to improve the reliability of the estimates and reduces the impact of reflections and other artefacts on the velocity estimates.

SWE uses ultrafast ultrasound techniques to track the propagation of the shear waves, both 10 kHz and 5 kHz frame rates have been used for imaging. Additionally, the voltage used has been 35 V (70 V peak-to-peak) for the single transducer and 30 V (60 V peak-to-peak) for the dual transducer setup, which means there's potentially a lot of energy produced. The thermal measurements showed that transducer and patient safety is a serious concern with the current system. In air the transducer temperature increased by 10 °C in a matter of seconds, and with an SSI sequence consisting of an imaging PRF of 5 kHz, 5 ARF pushes and 10 ms of imaging at a rate of 5 sequences per second, the temperature increased by 10 °C in less than 5 minutes on a PVA phantom.

5.1 Limitations

While this report has presented methods capable of differentiating between different tissue stiffnesses in heterogeneous mediums, the methods are not applicable to clinical trials without further testing and adjustments to the setup. Additionally, the performance of the methods presented have not been optimized for real-time applications. The cross-correlation method can be very slow (>5 minutes) depending on the parameters used, a version of the line detection algorithm was implemented on the Verasonics system and was running "real-time", but every velocity map took about 2-3 seconds to process. On the other hand, the full-width cross-correlation took about 10 seconds to process and achieved better results than the first cross-correlation method. It's quite safe to assume that faster performance can be achieved through smart choice of parameters and algorithm tinkering, but in the current state, the algorithms presented are not particularly suited for real-time.

Every measurement and estimation based on the heterogeneous phantom is based on an assumption that it's based on two mostly homogeneous mediums with an expectaction that they are distinct from each other. At the same time the phantom clearly has a lot artifacts and is not uniform in the B-mode images, this makes it very difficult to know if unexpected velocity estimations are a limitation of the algorithm or simply features of the phantom. The multi-purpose phantom alleviated some of those concerns, proving that reasonable estimates can be found in a known heterogeneous mediums, even so there will always be some uncertainty associated with the expectations of the heterogeneous phantom.

5.2 Future work

While *in vitro* tests were successfully able to identify cysts and provide quantitative estimates of the stiffness in ultrasound phantoms, more work and testing is necessary to ensure patient safety before *in vivo* tests can be performed. The thermal measurements suggest that the current setup generates too much heat for use on patients. Reducing the voltage used for the imaging sequence could be an option, also reducing the PRF. The impact of different SSI sequences on the heat generation was not considered in the thermal measurements presented here, but a thorough assessment of different parameters impact on patient safety, i.e. thermal index (TI) and mechanical index (MI), would be necessary before clinical use. Some parameters that would be relevant to consider include: imaging PRF, pulse lengths (both imaging and ARF pulse), frequency, frame rate, voltage/amplitude of imaging pulses, number of active transducer elements, and the duration of the imaging sequence.

The elasticity estimations of the multi-purpose phantom were able to identify the cysts, even though they were much harder to spot in the B-mode image. However the quantitative estimates were all wrong, the stiffness was biased towards the surrounding medium. As mentioned previously, the bias might be caused by the great distance between the cross-correlated sequences combined with a relatively small cyst. Those cysts in the multi-purpose phantom were the only parts with known elasticity in this project, as a result it is hard to say how good the methods are as estimators for tissue stiffness. Some testing and possibly "calibration" with known elasticities would be a natural next step to ensure that it's a good estimator. It might be a biased estimator, but that's fine if the bias is reliable.

The dual transducer setup presented in this report is rather simple, excite shear waves with one probe and image them with the other. And while this setup can be useful image shear waves in hard to reach areas, there are many possible uses that remain unexplored. It would be possible to use both transducers to gain more information, potentially even image the 3D propagation of the shear wave. That would require further work on post-processing algorithms to accomplish, and possibly also information about the positioning of the transducers relative to each other. Information about positioning is also relevant for regular quantitative estimates with two transducers, considering the angle of the transducer relative to the shear wave propagation has direct impact on the estimated shear wave velocity. The dual transducer setup also makes it possible to image the behaviour of the shear wave over greater distance, testing the range of the shear waves would be an interesting way to assess the improved signal strength from SSI sequences.

Other methods that have been used in SWE that could be worth considering includes pulse inversion of the imaging pulses to improve imaging SNR through harmonic imaging. Apodization is also a common technique that can improve the results, apodization of the imaging pulses is particularly common, but ARFI apodization can be considered as well. In this project neither were applied.

Chapter 6

Conclusion

This report has presented an implementation of SWE using SSI on an ultrasound research system. It was found that the multiple shear wave sources used in SSI both improved SNR and insonified a larger area. 5 mm intervals between the focal points of the ARF pulses, with a PRF of 5 kHz and medium with a shear wave velocity of ~4 m/s, were found to give a good range without an excessive number of ARF pulses, and a plane wavefront. Although many other SSI parameters are also perfectly reasonable.

Several different algorithms for estimating shear wave velocity were presented. Methods based on line detection were found to be relatively fast, but with poor resolution making them less desirable for heterogeneous mediums. Cross-correlation methods had far better spatial resolution and were better suited for heterogeneous mediums. In most cases, the "full-width" cross-correlation method using the maximum length of the correlation segments are the best option. It showed better or similar performance in all cases, and the implementation used was significantly faster than the other cross-correlation methods.

The dual transducer setup was able to excite and image shear waves with different transducers. The setup showed that it was capable of estimating shear wave velocity, and by extension shear elasticity in the same way as the single transducer setup. No compensation for the relative angle of the imaging transducer was made, which would be necessary in order to obtain accurate quantitave estimates with this setup. Due to space limitations on the PVA phantom, only rudimentary measurements were made with the dual transducer setup. It would be desirable to assess how the shear wave propagates over longer distances, or at different angles (e.g. in elevation direction), but this was not assessed.

Bibliography

[1] K. R. Nightingale, M. L. Palmeri, R. W. Nightingale, and G. E. Trahey, "On the feasibility of remote palpation using acoustic radiation force", *The Journal of the Acoustical Society of America*, vol. 110, no. 1, pp. 625–634, 2001, Basic ARFI, discusses safety considerations like TI.

[2] A. D'Amico and R. Pittenger, "A brief history of active sonar", DTIC Document, Tech. Rep., 2009.

[3] K. T. Dussik, "Über die möglichkeit, hochfrequente mechanische schwingungen als diagnostisches hilfsmittel zu verwerten", *Zeitschrift für die gesamte Neurologie und Psychiatrie*, vol. 174, no. 1, pp. 153–168, 1942.

[4] J. P. Baker, "The history of sonographers", *Journal of ultrasound in medicine*, vol. 24, no. 1, pp. 1–14, 2005.

[5] T. L. Szabo, *Diagnostic ultrasound imaging: Inside out.* Academic Press, 2004.

[6] S. Dixon, *Diagnostic imaging dataset - annual statistical release 2015/16*, NHS England, Prepared by: Operational Information for Commisioning, Oct. 2016.

[7] L. Gao, K. Parker, R. Lerner, and S. Levinson, "Imaging of the elastic properties of tissue—a review", *Ultrasound in medicine & biology*, vol. 22, no. 8, pp. 959–977, 1996.

[8] B. Castaneda, K. Hoyt, K. Westesson, L. An, J. Yao, L. Baxter, J. Joseph, J. Strang, D. Rubens, and K. Parker, "Performance of three-dimensional sonoelastography in prostate cancer detection: A comparison between ex vivo and in vivo experiments", in *Ultrasonics Symposium (IUS), 2009 IEEE International*, IEEE, 2009, pp. 519–522.

[9] L. Pallwein, M. Mitterberger, G. Pinggera, F. Aigner, F. Pedross, J. Gradl, A. Pelzer, G. Bartsch, and F. Frauscher, "Sonoelastography of the prostate: Comparison with systematic biopsy findings in 492 patients", *European journal of radiology*, vol. 65, no. 2, pp. 304–310, 2008.

[10] S. Chen, M. W. Urban, C. Pislaru, R. Kinnick, Y. Zheng, A. Yao, and J. F. Greenleaf, “Shearwave dispersion ultrasound vibrometry (sduv) for measuring tissue elasticity and viscosity”, *IEEE transactions on ultrasonics, ferroelectrics, and frequency control*, vol. 56, no. 1, pp. 55–62, 2009.

[11] J. M. Chang, W. K. Moon, N. Cho, A. Yi, H. R. Koo, W. Han, D.-Y. Noh, H.-G. Moon, and S. J. Kim, “Clinical application of shear wave elastography (swe) in the diagnosis of benign and malignant breast diseases”, *Breast cancer research and treatment*, vol. 129, no. 1, pp. 89–97, 2011.

[12] W. A. Berg, D. O. Cosgrove, C. J. Doré, F. K. Schäfer, W. E. Svensson, R. J. Hooley, R. Ohlinger, E. B. Mendelson, C. Balu-Maestro, M. Locatelli, *et al.*, “Shear-wave elastography improves the specificity of breast us: The be1 multinational study of 939 masses”, *Radiology*, vol. 262, no. 2, pp. 435–449, 2012.

[13] D. O. Cosgrove, W. A. Berg, C. J. Doré, D. M. Skyba, J.-P. Henry, J. Gay, C. Cohen-Bacrie, B. S. Group, *et al.*, “Shear wave elastography for breast masses is highly reproducible”, *European radiology*, vol. 22, no. 5, pp. 1023–1032, 2012.

[14] H. L. Oestreicher, “Field and impedance of an oscillating sphere in a viscoelastic medium with an application to biophysics”, *The Journal of the Acoustical Society of America*, vol. 23, no. 6, pp. 707–714, 1951.

[15] R. M. Lerner, S. Huang, and K. J. Parker, ““sonoelasticity” images derived from ultrasound signals in mechanically vibrated tissues”, *Ultrasound in medicine & biology*, vol. 16, no. 3, pp. 231–239, 1990.

[16] Y. Yamakoshi, J. Sato, and T. Sato, “Ultrasonic imaging of internal vibration of soft tissue under forced vibration”, *IEEE transactions on ultrasonics, ferroelectrics, and frequency control*, vol. 37, no. 2, pp. 45–53, 1990.

[17] T. Sugimoto, S. Ueha, and K. Itoh, “Tissue hardness measurement using the radiation force of focused ultrasound”, in *Ultrasonics Symposium, 1990. Proceedings., IEEE 1990*, IEEE, 1990, pp. 1377–1380.

[18] M. Fatemi and J. F. Greenleaf, “Ultrasound-stimulated vibro-acoustic spectrography”, *Science*, vol. 280, no. 5360, pp. 82–85, 1998.

[19] A. P. Sarvazyan, O. V. Rudenko, S. D. Swanson, J. B. Fowlkes, and S. Y. Emelianov, “Shear wave elasticity imaging: A new ultrasonic technology of medical diagnostics”, *Ultrasound in medicine & biology*, vol. 24, no. 9, pp. 1419–1435, 1998.

[20] J. Bercoff, M. Tanter, and M. Fink, “Supersonic shear imaging: A new technique for soft tissue elasticity mapping”, *IEEE transactions on ultrasonics, ferroelectrics, and frequency control*, vol. 51, no. 4, pp. 396–409, 2004.

[21] K. Nightingale, S. McAleavey, and G. Trahey, “Shear-wave generation using acoustic radiation force: In vivo and ex vivo results”, *Ultrasound in medicine & biology*, vol. 29, no. 12, pp. 1715–1723, 2003.

[22] K. Parker, S. Huang, R. Musulin, and R. Lerner, “Tissue response to mechanical vibrations for “sonoelasticity imaging””, *Ultrasound in medicine & biology*, vol. 16, no. 3, pp. 241–246, 1990.

[23] A. Caenen, D. Shcherbakova, B. Verhegghe, C. Papadacci, M. Pernot, P. Segers, and A. Swillens, “A versatile and experimentally validated finite element model to assess the accuracy of shear wave elastography in a bounded viscoelastic medium”, *IEEE transactions on ultrasonics, ferroelectrics, and frequency control*, vol. 62, no. 3, pp. 439–450, 2015.

[24] T. Nordenfur, “Comparison of pushing sequences for shear wave elastography”, Master’s thesis, Royal Institute of Technology (KTH), Stockholm, Sweden, 2013.

[25] M. Tanter, J. Bercoff, A. Athanasiou, T. Deffieux, J.-L. Gennisson, G. Montaldo, M. Muller, A. Tardivon, and M. Fink, “Quantitative assessment of breast lesion viscoelasticity: Initial clinical results using supersonic shear imaging”, *Ultrasound in medicine & biology*, vol. 34, no. 9, pp. 1373–1386, 2008.

[26] P. Song, H. Zhao, M. W. Urban, A. Manduca, S. V. Pislaru, R. R. Kinnick, C. Pislaru, J. F. Greenleaf, and S. Chen, “Improved shear wave motion detection using pulse-inversion harmonic imaging with a phased array transducer”, *IEEE transactions on medical imaging*, vol. 32, no. 12, pp. 2299–2310, 2013.

[27] J. Bercoff, *Ultrafast ultrasound imaging.* INTECH Open Access Publisher, 2011.

[28] G. Montaldo, M. Tanter, J. Bercoff, N. Benech, and M. Fink, “Coherent plane-wave compounding for very high frame rate ultrasonography and transient elastography”, *IEEE transactions on ultrasonics, ferroelectrics, and frequency control*, vol. 56, no. 3, pp. 489–506, 2009.

[29] Bansal and R.K., “A textbook of fluid mechanics and hydraulic machines”, in. Laxmi Publications, 2005, ch. 15, p. 709, ISBN: 8131808157.

[30] M. Tanter, J. Bercoff, L. Sandrin, and M. Fink, “Ultrafast compound imaging for 2-d motion vector estimation: Application to transient elastography”, *IEEE transactions on ultrasonics, ferroelectrics, and frequency control*, vol. 49, no. 10, pp. 1363–1374, 2002.

[31] C. Kasai, K. Namekawa, A. Koyano, and R. Omoto, “Real-time two-dimensional blood flow imaging using an autocorrelation technique”, *IEEE Trans. Sonics Ultrason*, vol. 32, no. 3, pp. 458–464, 1985.

[32] O. Bonnefous and P. Pesque, “Time domain formulation of pulse-doppler ultrasound and blood velocity estimation by cross correlation”, *Ultrasonic imaging*, vol. 8, no. 2, pp. 73–85, 1986.

[33] M. Sharifi, M. Fathy, and M. T. Mahmoudi, “A classified and comparative study of edge detection algorithms”, in *Information Technology: Coding and Computing, 2002. Proceedings. International Conference on*, IEEE, 2002, pp. 117–120.

[34] D. Marr and E. Hildreth, “Theory of edge detection”, *Proceedings of the Royal Society of London B: Biological Sciences*, vol. 207, no. 1167, pp. 187–217, 1980.

[35] H. P. VC, *Method and means for recognizing complex patterns*, US Patent 3,069,654, Dec. 1962.

[36] R. O. Duda and P. E. Hart, “Use of the hough transformation to detect lines and curves in pictures”, *Communications of the ACM*, vol. 15, no. 1, pp. 11–15, 1972.

[37] M. Marxen, P. Sullivan, M. Loewen, and B. Jähne, “Comparison of gaussian particle center estimators and the achievable measurement density for particle tracking velocimetry”, *Experiments in Fluids*, vol. 29, no. 2, pp. 145–153, 2000.

[38] F. Foster, M. Patterson, M. Arditi, and J. Hunt, “The conical scanner: A two transducer ultrasound scatter imaging technique”, *Ultrasonic imaging*, vol. 3, no. 1, pp. 62–82, 1981.

[39] J. Fromageau, J.-L. Gennisson, C. Schmitt, R. L. Maurice, R. Mongrain, and G. Cloutier, “Estimation of polyvinyl alcohol cryogel mechanical properties with four ultrasound elastography methods and comparison with gold standard testings”, *IEEE transactions on ultrasonics, ferroelectrics, and frequency control*, vol. 54, no. 3, 2007.

[40] T. J. Hall, M. Bilgen, M. F. Insana, and T. A. Krouskop, “Phantom materials for elastography”, *Ieee transactions on ultrasonics, ferroelectrics, and frequency control*, vol. 44, no. 6, pp. 1355–1365, 1997.

[41] W. D. D’Souza, E. L. Madsen, O. Unal, K. K. Vigen, G. R. Frank, and B. R. Thomadsen, “Tissue mimicking materials for a multi-imaging modality prostate phantom”, *Medical physics*, vol. 28, no. 4, pp. 688–700, 2001.